Australian Journal of Earth Sciences

An International Geoscience Journal of the Geological Society of Australia

ISSN: (Print) (Online) Journal homepage: www.tandfonline.com/journals/taje20

The Permian Watershed tungsten deposit (northeast Queensland, Australia): fluid inclusion and stable isotope constraints

J. A. Poblete, J-M. Huizenga, Z. Chang & P. Dirks

To cite this article: J. A. Poblete, J-M. Huizenga, Z. Chang & P. Dirks (01 Sep 2024): The Permian Watershed tungsten deposit (northeast Queensland, Australia): fluid inclusion and stable isotope constraints, Australian Journal of Earth Sciences, DOI: 10.1080/08120099.2024.2390686

To link to this article: https://doi.org/10.1080/08120099.2024.2390686

© 2024 The Author(s). Published by Informa UK Limited, trading as Taylor & Francis Group

View supplementary material

Published online: 01 Sep 2024.

Submit your article to this journal

View related articles

View Crossmark data

Full Terms & Conditions of access and use can be found at
https://www.tandfonline.com/action/journalInformation?journalCode=taje20

AUSTRALIAN JOURNAL OF EARTH SCIENCES
https://doi.org/10.1080/08120099.2024.2390686

OPEN ACCESS Check for updates

The Permian Watershed tungsten deposit (northeast Queensland, Australia): fluid inclusion and stable isotope constraints

J. A. Poblete[a,b], J-M. Huizenga[a,c,d], Z. Chang[a,e] and P. Dirks[a]

[a]Economic Geology Research Centre, College of Science and Engineering, James Cook University, Townsville, QLD, Australia; [b]W.H. Bryan Geology and Mining Centre, Sustainable Minerals Institute, Indooroopilly, QLD, Australia; [c]Faculty of Environmental Sciences and Natural Resource Management, Norwegian University of Life Sciences, Ås, Norway; [d]Department of Geology, University of Johannesburg, Johannesburg, South Africa; [e]Department of Geology and Geological Engineering, Colorado School of Mines, Golden, CO, USA

ABSTRACT

The Watershed scheelite deposit is located in an extinct fore-arc basin in the Mossman Orogen of North Queensland. This fore-arc region comprises multiply deformed, Ordovician–Silurian metasedimentary rocks of the Hodgkinson Formation, and it was intruded by Carboniferous–Permian granites of the Kennedy Igneous Association. At Watershed, the Hodgkinson Formation includes strongly deformed skarn-altered conglomerate, psammite and slate units, which record four deformation events that evolved from ductile (D_{1-3}) to brittle–ductile (D_4). Early, D_{1-2} scheelite mineralisation in Carboniferous monzonite and skarn-altered conglomerate formed during regional prograde metamorphism, which reached upper greenschist to lower amphibolite facies conditions. Permian, D_4 scheelite mineralisation was deposited in transtensional, shear-related veins, vein haloes and skarn-altered conglomerate during retrograde, lower greenschist facies metamorphism. During D_4, four stages of retrograde alteration (retrograde stages 1–4) affected the rocks. Fluid inclusion assemblages in retrograde stage 2, vein scheelite and quartz are characterised by a low-salinity H_2O–NaCl ± CH_4 fluid (XCH_4 <0.01, 1.4–8.0 wt% $NaCl_{eq}$). The fluid inclusions show evidence for fluid mixing between a low (~0 wt% $NaCl_{eq}$) and a medium (<8 wt% $NaCl_{eq}$) saline fluid. Scheelite mineralisation *P–T* conditions were determined at ~300 °C and 1–1.8 kbar (*i.e.* a depth of 3.7–6.7 km), indicative of a high geothermal gradient (35–75 °C/km), which was likely caused by the heat from the Permian granites. The presence of pyrrhotite and arsenopyrite in D_4 veins (retrograde stage 4), plus graphite and methane in the fluid inclusions in scheelite, indicates reduced mineralisation conditions. Oxygen isotope compositions ($\delta^{18}O_{VSMOW}$) of retrograde stage 2 scheelite (+3.8 to +7.3‰), plagioclase (+7.0 to +11.8‰) and quartz (+12.6 to +15.5‰) indicate a fluid temperature of 306 ± 56 °C with $\delta^{18}O_{VSMOW}$ values between +4.7 and +8.3‰. Retrograde stage 3 muscovite δD_{VSMOW} (−73.4 to −62.7‰) and $\delta^{18}O_{VSMOW}$ (+11.5 to +13.2‰) values were used to calculate the O–H isotopic compositions of the fluids in equilibrium with the minerals at various possible temperatures (250–300 °C). The results are consistent with a metamorphic origin for the mineralising fluid. Sulfur isotope compositions ($\delta^{34}S_{CDT}$ between −2.5 and +2.8‰) for vein-hosted, retrograde stage 4 sulfides indicate that sulfur could have come from seawater or seawater sulfate, which is consistent with the local geology, even though this range overlaps with magmatic sulfur isotope compositions. Metamorphic fluids probably originated from devolatilisation reactions in the Hodgkinson Formation during prograde metamorphism. Permian intrusions acted as heat source enhancing metamorphic fluid flow and metal transport.

KEY POINTS

The main economic D_4 scheelite mineralisation in veins occur at temperatures of 306 ± 56 °C and depths between 3.7 and 6.7 km.

1. D_4 scheelite mineralisation precipitated predominantly from a low- to medium-salinity metamorphic fluid, and with both H_2O–NaCl and H_2O–NaCl–CH_4 compositions.
2. The presence of methane (CH_4) plus graphite in some fluid inclusions and the sulfide mineral phases indicates reduced mineralisation conditions.

ARTICLE HISTORY
Received 30 June 2023
Accepted 28 July 2024

KEYWORDS
tungsten; fluid inclusions; stable isotopes; metamorphic scheelite; critical mineral; Permian

Introduction

Tungsten is considered a strategic metal by many countries around the world. It has unique physical and chemical properties, such as the highest melting point of all metals (3422 °C) and a high density like Au (19.3 g/cm^3) and can be combined with carbon to make tungsten carbide, which is nearly as hard as diamond (*i.e.* a Mohr hardness scale of 9). Thus, tungsten cannot be easily substituted in many of its applications in modern technologies (*e.g.* cemented carbide, mill products, steel/

CONTACT J. A. Poblete japoblet@gmail.com Economic Geology Research Centre, College of Science and Engineering, James Cook University, Townsville, QLD 4811, Australia

Supplemental data for this article can be accessed online at https://doi.org/10.1080/08120099.2024.2390686.
Editorial handling: Carl Sandler

© 2024 The Author(s). Published by Informa UK Limited, trading as Taylor & Francis Group
This is an Open Access article distributed under the terms of the Creative Commons Attribution-NonCommercial-NoDerivatives License (http://creativecommons.org/licenses/by-nc-nd/4.0/), which permits non-commercial re-use, distribution, and reproduction in any medium, provided the original work is properly cited, and is not altered, transformed, or built upon in any way. The terms on which this article has been published allow the posting of the Accepted Manuscript in a repository by the author(s) or with their consent.

alloy, aviation, lamp and electronic industries) and others such as sport and leisure (*e.g.* horse riding, biking or trekking).

The Watershed tungsten deposit is situated in the central Mossman Orogen in northeast Queensland (Australia). The deposit is hosted by strongly deformed Silurian–Devonian, metasedimentary rocks (Henderson *et al.*, 2013), which were intruded by Carboniferous–Permian, S-type granites (Champion & Bultitude, 2013; Figure 1). The Watershed deposit has a resource of 70 000 t of WO_3 (49.3 Mt @ 0.14% WO_3; www.tungstenmining.com, 2024). Based on its alteration mineralogy, Watershed has been interpreted as a skarn-type deposit (Poblete *et al.*, 2021) that formed mainly from metamorphic, rather than magmatic hydrothermal fluids. This is unusual, as most skarns form from magmatic hydrothermal fluids (*e.g.* Meinert *et al.*, 2005 and references therein).

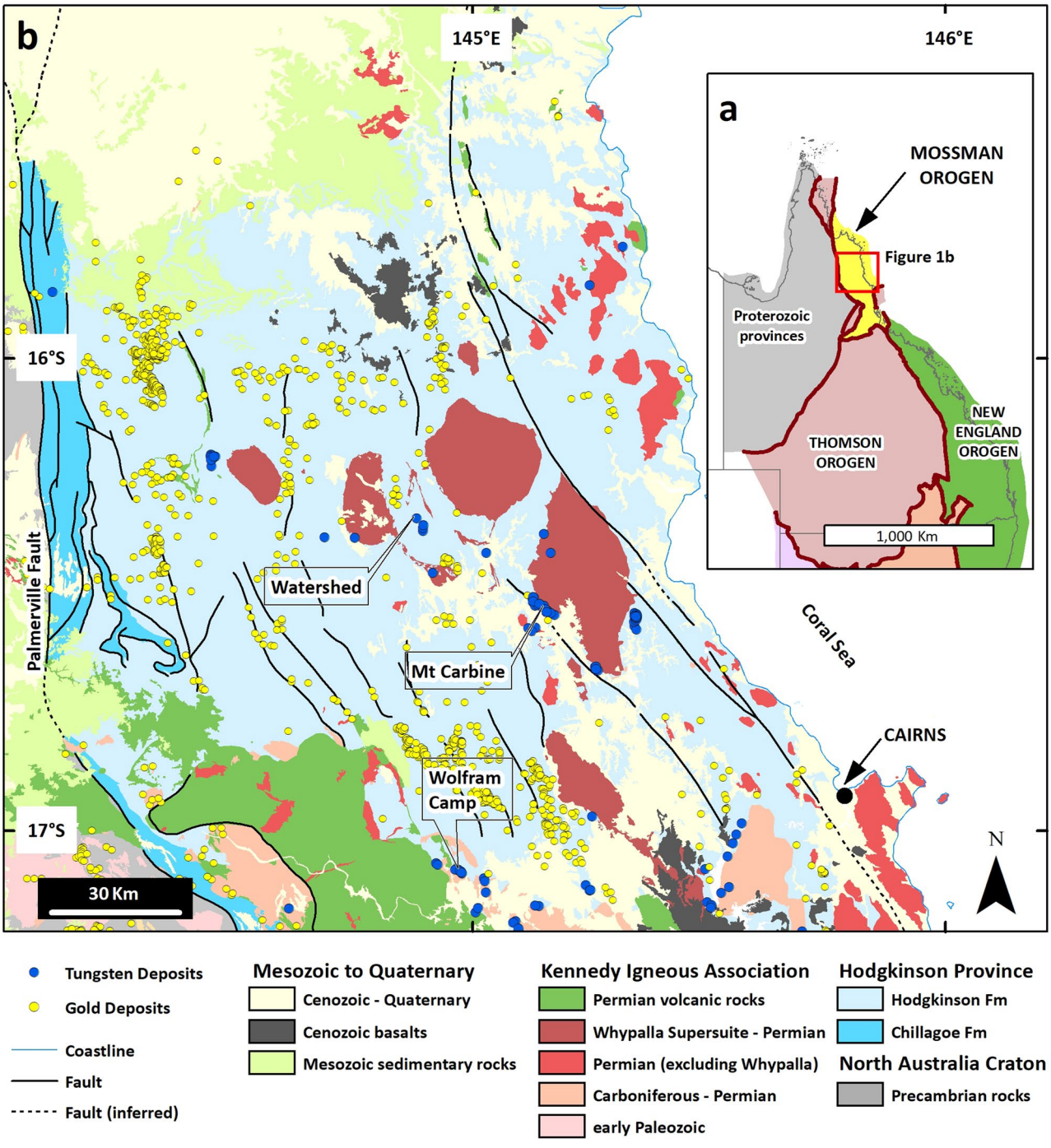

Figure 1. Regional geological setting of the Watershed deposit in North Queensland. (a) Different orogens of eastern Australia including the Mossman Orogen. The red square is enlarged in (b). (b) Geology of the Hodgkinson Province. The Permian volcanic rocks (green) and the Carboniferous–Permian (light orange) rocks of the Kennedy Igneous Province crop out to the south of the Hodgkinson Province. These rocks separate the Hodgkinson Province to the north from the Broken River Province to the south. Watershed is hosted by the Hodgkinson Formation and surrounded by S-type granites and syenogranites of the Permian Whypalla Supersuite. Significant tungsten deposits are indicated on the map, together with other tungsten and gold deposits, and occurrences hosted by the Hodgkinson Formation are also shown for reference.

Scheelite occurs in intrusion- and non-intrusion-related skarns that are the largest source of tungsten (Chang *et al*., 2019; Meinert *et al*., 2005; Newberry, 1998; Newberry & Swanson, 1986; Poblete *et al*., 2021) and in greisen deposits (Chang *et al*., 2017; Elliott *et al*., 1995). Scheelite is also a by-product or minor mineral in many orogenic gold deposits, where it formed synchronous with gold (Goldfarb *et al*., 2005; Groves, 1993; Henley *et al*., 1976; Peters *et al*., 1990). Published data on fluid inclusions hosted by scheelite in tungsten deposits are limited (Cattalani & Williams-Jones, 1991; Cheilletz, 1984; Schenk & Höll, 1991; So & Shelton, 1983), and most of the available data on mineralising fluids are derived from minerals associated with scheelite. Fluid-inclusion studies indicate that in granitoid-related tungsten deposits hosted in siliceous (carbonate-free) rocks, wolframite and scheelite deposit from mineralising fluids with salinities of less than 15 wt% $NaCl_{eq}$ at temperatures of 200–500 °C and pressures of 0.2–1.5 kbar (Wood & Samson, 2000). In tungsten skarn deposits associated with granitoids, aqueous fluid inclusions with salinities up to 61 wt% $NaCl_{eq}$ in scheelite record trapping temperatures and pressures of 280–600 °C and 0.5–1.5 kbar, respectively (Kwak, 1986). In some cases, formation depths greater than 8–10 km have been reported (*e.g.* Pine Creek skarn, California; Brown *et al*., 1985; Newberry, 1998).

In scheelite-bearing, metamorphic hydrothermal gold deposits, aqueous fluid inclusions hosted in quartz preserve homogenisation temperatures of 150–350 °C, which are lower than those recorded in granites and skarns (Goldfarb *et al*., 2005). The fluids have low salinities (<11 wt% $NaCl_{eq}$) and were trapped at crustal depths ranging from ~3 to >10 km (Bodnar *et al*., 2014; Goldfarb *et al*., 2005; Groves, 1993; Groves *et al*., 1998; Peters *et al*., 1990; Vos & Bierlein, 2006). Additional information on the source of mineralising fluids has been obtained from stable isotopes for ore and coexisting gangue minerals (Campbell & Larson, 1998; Shanks, 2014).

This paper presents the results of fluid-inclusion studies for quartz and scheelite from mineralised veins from Watershed that formed around *ca* 275 Ma during the main Permian mineralising events (Poblete *et al*., 2021). In addition, oxygen, hydrogen and sulfur isotope data for scheelite and related quartz, plagioclase, muscovite and sulfide grains are reported. The data allow us to obtain a better understanding of the physico-chemical conditions of the alteration and mineralisation processes. The data also supplement the geological observations (Poblete *et al*., 2021) and confirm the source(s) of the mineralising fluid(s).

Regional geology

The Watershed deposit is located in the central part of the Mossman Orogen, which formed within a late Paleozoic, active continental margin system abutting the North Australian Craton, from which it is separated by a major fault zone (Palmerville Fault). The Mossman Orogen is in fault contact with the Thomson Orogen to the south and the New England Orogen to the southeast (Donchak *et al*., 2013; Fergusson & Henderson, 2013; Figure 1a). The orogen consists of multiply deformed, sedimentary successions interpreted as turbidite sequences, with minor intercalations of mafic volcanic rocks and chert, deposited in a deep-marine environment (Henderson *et al*., 2013). The Mossman Orogen is composed of the Silurian to Devonian Hodgkinson Province in the north and Broken River Province in the south, which are exposed in a belt 500 km long and up to 200 km wide. The two provinces are separated from each other by Carboniferous to Permian granitoids of the Kennedy Igneous Association (Champion & Bultitude, 2013). The Hodgkinson Province is composed of the Hodgkinson Formation in the east and the Chillagoe Formation in the west. The Watershed deposit is hosted by rocks of the Hodgkinson Province (Figure 1b).

The Silurian to early Carboniferous Hodgkinson Formation (Adams *et al*., 2013; Kositcin *et al*., 2015; Figure 1b) includes alternating sandstone-mudstone beds that are locally interbedded with greywacke and quartz-greywacke units and rare intercalations of chert, volcanic rocks, limestone and polymictic conglomerate (Amos, 1968; de Keyser & Lucas, 1968). The Hodgkinson Formation is bounded to the west by the Silurian–Devonian Chillagoe Formation, which forms a narrow (2–5 km), north–south-trending zone that runs for ~250 km parallel to the Palmerville Fault (Figure 1b). Field relations and sedimentary textural characteristics indicate that the western and eastern portions of the Hodgkinson Formation represent the more proximal and distal facies, respectively, of a submarine fan delta system (Amos, 1968). The rocks of the Hodgkinson Formation were interpreted by Henderson *et al*. (2013) to have formed in a fore-arc environment containing rocks of the Silurian to Devonian Pama Igneous Association (Withnall & Hutton, 2013), which are mainly emplaced further west in the North Australia Craton (Figure 1a).

The Hodgkinson Formation has been affected by intense deformation. On a regional scale, four deformation events, D_1 to D_4, have been recognised (Davis, 1993; Henderson *et al*., 2013). D_1 is Devonian in age and coincident with peak metamorphism at low- to mid-greenschist facies in the southwest, grading to upper-greenschist–lower amphibolite facies in the northeast of the Hodgkinson Formation. A bedding-parallel slaty cleavage and variably plunging, mesoscale isoclinal folds characterise D_1. The second deformational event, D_2, is defined by large-scale folds with wavelengths of several kilometres, which formed during Devonian to early Carboniferous compressional events (Henderson *et al*., 2013). The third deformational event, D_3, is represented by a penetrative crenulation cleavage best developed in aureole zones of Permian granitoids and considered to have formed as a subhorizontal cleavage during early Permian extension (Davis & Henderson, 1999). Structures assigned to D_4 are more localised and variable in nature and tend to be co-planar with D_2 structures making their recognition difficult. Deformation during D_4 has been linked to the formation of mesoscopic folds, and it is associated with a north–south-trending crenulation cleavage that is best developed near Permian granitoid plutons (Davis *et al*., 2002). This deformation is linked to compressional events during the late Permian.

The rocks of the Hodgkinson Formation were intruded by late Carboniferous to Permian granites assigned to the Kennedy Igneous Association (Champion & Bultitude, 2013; Figure 1b). In

the northern portion of the Hodgkinson Province, these intrusions are represented by ~4000 km^2 of outcrop of Permian, mainly S-type granites assigned to the Daintree Subprovince (Mackenzie & Wellman, 1997). The Daintree Subprovince has been further subdivided based on geochemical characteristics (Bultitude & Champion, 1992). Watershed is surrounded by S-type granites assigned to the early Permian Whypalla Supersuite (Figure 1b), which were emplaced during D_4 (Davis, 1993) around 285–260 Ma (Champion & Bultitude, 2013; Poblete *et al*., 2021). The granites of the Whypalla Supersuite are porphyritic to equigranular in texture, and mainly consist of muscovite–biotite syenogranite and monzogranite with rare granodiorite (Bultitude & Champion, 1992).

Geology of the Watershed deposit

The rocks in the Watershed area consist of metasedimentary units assigned to the Hodgkinson Formation and comprise psammite, polymictic skarn-altered conglomerate, slate and slate–siltstone breccia, with minor quartzite and rare chert (Figures 2 and 3). Psammite is the most common rock type (Figure 2) and is light to dark grey, composed of fine- to medium-grained (<2 mm), angular to subrounded quartz grains (45 vol%), euhedral to subhedral plagioclase grains (40 vol%), and minor (5 vol%), fine-grained biotite (Figure 4a). The matrix consists of fine-grained quartz, plagioclase, biotite and muscovite. Polymictic, skarn-altered conglomerate occurs interlayered with the psammite (Figures 2 and 3) as isolated pod-like bodies and layer fragments, <15 m wide and tens of metres in length. This rock type contains subrounded pebbles, 3–30 cm in diameter, that preserve a skarn mineralogy (Poblete *et al*., 2021; Figure 4b). This unit is the main host for disseminated and vein-type scheelite mineralisation (Figure 3). A few quartzite beds are dispersed within the psammite unit (Figure 3) and are composed of a medium-grained, dark grey rock, dominated by 2–5 mm large, subrounded quartz grains (>70 vol%) with minor biotite and feldspar (Figure 4c). Strongly deformed slate and slate–siltstone breccia units are widespread within Watershed and its immediate surroundings (Figures 2 and 3). Foliated slate is present as massive units interbedded with 0.5–20 cm-thick siltstone layers. Slate–siltstone breccia is typically composed of isolated fragments (10–90 vol%) of sandstone (Figure 4d) and siltstone that are 0.5–5 cm in size and set in a strongly foliated, dark grey matrix of mudstone (slate), defining an intense linear fabric. Thinly banded, black to grey chert beds form a minor unit within the slate–siltstone breccia.

The metasedimentary rocks at Watershed are strongly deformed with intense folding and at least three penetrative foliations that are best developed in the slate and slate–siltstone breccia units (Figure 4d). In psammite and polymictic, skarn-altered conglomerate the deformation events resulted in extension and the formation of a dominant mineral lineation, defined by boudin trails and layer segments enveloped by slate and slate–siltstone breccia units (Figure 2). The primary layering was generally destroyed in the fine-grained slate units and slate–siltstone breccia, but it is locally preserved within psammite boudins and as conglomerate layer segments. The semi-continuous boudin trails of skarn-altered conglomerate provide evidence for primary layering (Figure 2). The first two deformational events (D_{1-2}) coincided with peak metamorphism (Figure 5) and involved complete, and probably repeated, transposition of the primary layering associated with upright isoclinal folding, and the formation of a penetrative, steeply southwest-dipping foliation (S_1/S_2; Poblete *et al*., 2021). The third deformational event, D_3, is represented by cm- to km-scale tight to open, upright folds that fold the S_1/S_2 transposition fabric. D_3 folds are locally associated with a near-vertical, north-northwest-trending axial planar crenulation cleavage (S_3; Poblete *et al*., 2021). Late brittle-ductile D_4 shear zones cut and displace the D_1–D_3 fabrics. The D_4 shear zones are generally narrow (<10 cm wide) except for a major near-vertical D_4 shear zone with a steeply plunging, near down-dip lineation, which occurs along the eastern margin of Watershed (Poblete *et al*., 2021; Figure 2). Around Watershed, the narrow D_4 shear zones display a wide variety of orientations, but they are generally parallel to the main north-northwest to north-trending, ductile, S_{1-2} fabric. The narrow D_4 shear zones are near vertical (Figure 3) and preserve a dextral sense of movement (Poblete *et al*., 2021). Numerous smaller fractures and shears in the vicinity of major shear zones display a greater variation of orientations, and a normal movement sense is common. The shear zones are spatially associated with economic scheelite mineralisation in veins and in alteration zones where they transect skarn-altered conglomerate (Poblete *et al*., 2021).

The metasedimentary rocks at Watershed are intruded by Carboniferous and Permian dykes assigned to the Whypalla Supersuite (Poblete *et al*., 2021; Figures 2 and 3). The Carboniferous dykes are *ca* 350 Ma in age and monzonitic in composition (Poblete *et al*., 2021). They have not been found in outcrop, but they can be seen in drill core where they occur as less than 40 cm wide, dark to light-grey dykes that contain a foliation (S_{1-2}), indicating that they were emplaced and deformed early in the deformation history of the area (Figure 3b). Felsic minerals include 55 vol% sub- to euhedral plagioclase (<0.5 mm), 35 vol% subhedral K-feldspar (<0.5 mm) and ~5 vol% anhedral quartz. Mafic minerals correspond to ~5 vol% of the rock and consist entirely of subhedral biotite (<0.5 mm; Figure 4e). These dyke segments are economically important, because they contain 10–15 vol% euhedral and partly resorbed to strongly fractured scheelite crystals (Figure 4f, see below) that were affected by recrystallisation events following the formation of the S_{1-2} fabric. This generation of scheelite occurs in close association with oligoclase (Poblete *et al*., 2021; Figure 5). Younger Permian dykes (*ca* 275 Ma) are granitic in composition and crop out across the Watershed area (Poblete *et al*., 2021; Figure 2). These undeformed granite dykes cut the D_1 to D_3 ductile fabrics and appear to postdate the D_4 shear zones. They vary in width from 0.5 m to several tens of metres and can be traced along strike for tens to hundreds of metres. They show varied textures and include coarse porphyritic (Figure 4g) to fine-grained varieties. The porphyritic dykes comprise phenocrysts of K-feldspar (20 vol%), quartz (20 vol%) and plagioclase (5 vol%) in a groundmass of fine-grained quartz, K-feldspar and muscovite, which occur in approximately equal amounts.

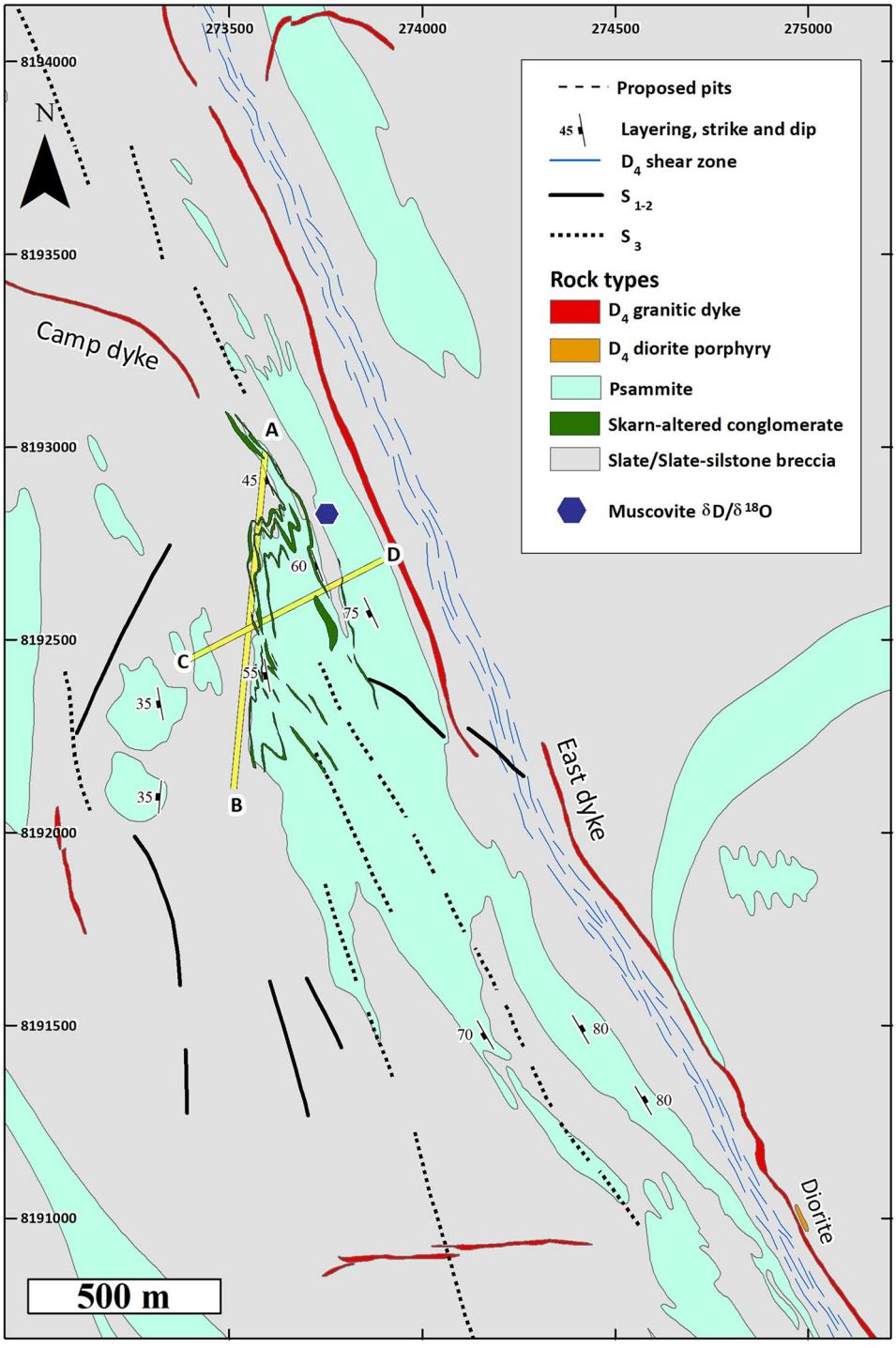

Figure 2. Generalised geological map of the Watershed deposit, showing the location of the muscovite sample WS16-006. Note that the skarn-altered conglomerate follows the regional fabric and shows transposition. A–B and C–D refer to cross-sections shown in Figure 3. Base map from Skrzeczynski and Wood (1984). The grid system is Geocentric Datum of Australia 1994 (GDA94), zone 55.

Scheelite mineralisation

Scheelite mineralisation at Watershed is related to two events (Poblete *et al*., 2021); an early Carboniferous intrusive-related event at *ca* 350 Ma, overprinted by a later Permian metamorphic hydrothermal event at *ca* 275 Ma. Early disseminated scheelite mineralisation is aligned in S_{1-2} and occurs in close spatial association with the *ca* 350 Ma monzonite dykes. The bulk of the scheelite mineralisation at Watershed occurs in D_4, transtensional quartz–plagioclase veins where they crosscut skarn-altered conglomerate of the Hodgkinson Formation. Early D_{1-2} scheelite mineralisation is found disseminated in monzonite and in skarn-altered conglomerate where it formed during prograde and peak metamorphism (Figures 4f, h and 5). Later, retrograde D_4 scheelite occurs as stringers in skarn-altered

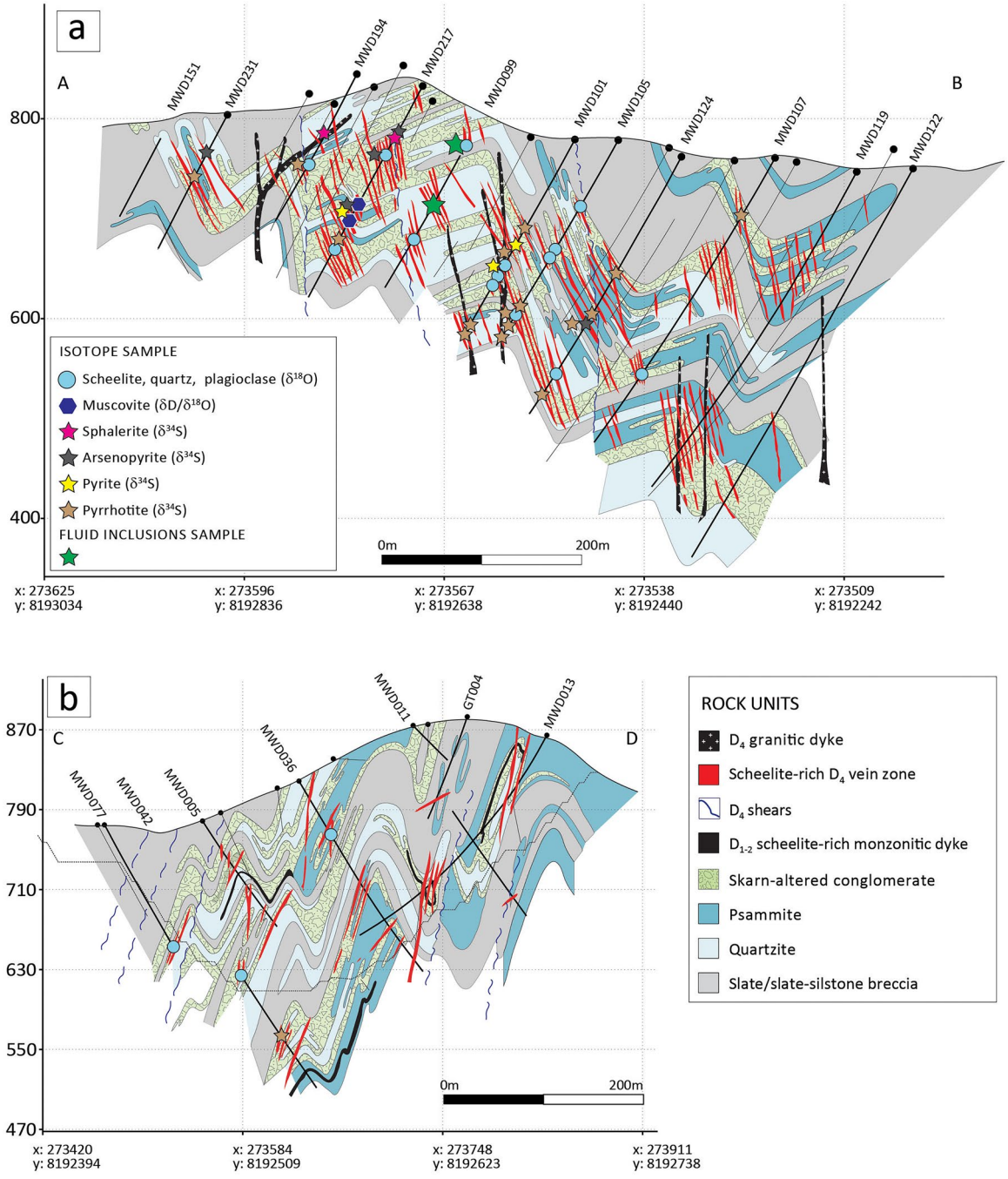

Figure 3. Generalised sections through the Watershed deposit showing chosen samples used for isotopes and fluid inclusion studies. (a) NNE (008°) long section looking east. Syn-D_4 veins are visible in this section since the main orientation of these veins is east–west. (b) Cross-section (055°) looking north. The early D_{1-2} and D_3 deformation events and related transposition are clearly visible, since the σ_1 has a preferential east–west orientation (Poblete *et al.*, 2021). See Figure 2 for the section locations. The grid system is Geocentric Datum of Australia 1994 (GDA94), zone 55.

conglomerate, and along the margins and in alteration haloes of multi-staged, syn-D_4 quartz–plagioclase veins in skarn-altered conglomerate (Figure 4i). Based on cross-cutting relationships, the D_4 retrograde events have been subdivided into four stages (Poblete *et al.*, 2021; Figure 5).

Syn-D_{1-2} scheelite mineralisation

Syn-D_{1-2}, sub- to euhedral scheelite crystals in monzonite dykes (Figure 4f) are <2 mm in diameter and are generally strongly fractured. They display complex growth zoning, dissolution lamellae and resorbed boundaries, which suggest partial recrystallisation during later deformation (Poblete *et al.*, 2021). Scheelite grains also exhibit ductile deformation features such as sigmoidal or boudin shapes, and in places scheelite trails were folded during D_3 (Figure 4f, h) indicating that scheelite mineralisation pre-dated D_3.

Disseminated D_{1-2} scheelite in polymictic, skarn-altered conglomerate aligns with the S_{1-2} foliation (Figure 4h). The foliation is characterised by quartz-rich patches, with scheelite coexisting with

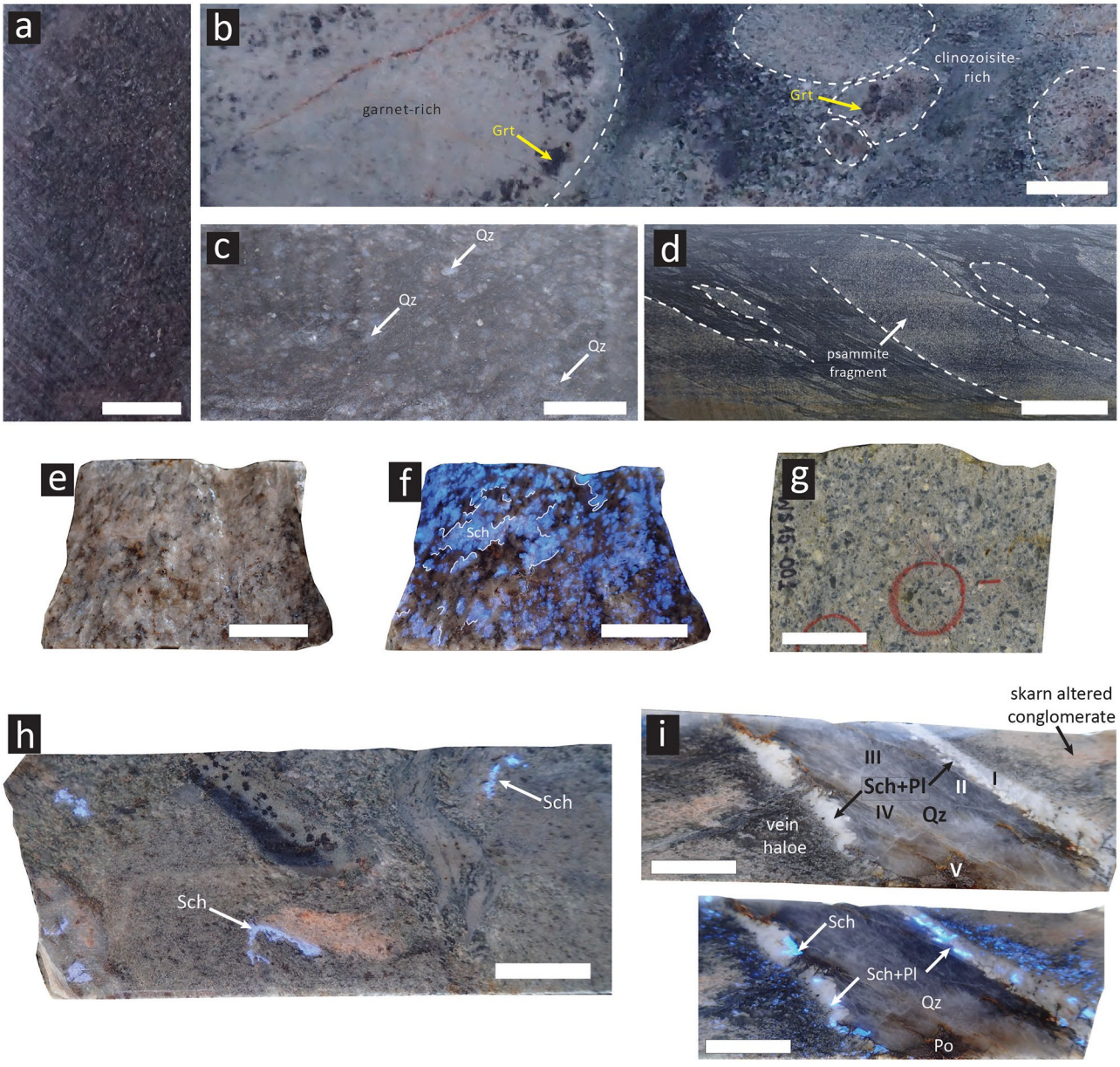

Figure 4. Hand specimen sample photographs of the different rock types at the Watershed deposit. For sample locations, see Figure 3. Mineral abbreviations are from Whitney and Evans (2010). White rectangles are 2 cm scale bars in each image. (a) Psammite from drill core MWD124 at 216 m. (b) Skarn-altered conglomerate from drill core MWD101 at 159 m. (c) Quartzite from drill core MWD099 at 150 m. (d) Slate–siltstone breccia from drill core MWD119 at 20 m. (e) Monzonitic dyke from drill core MWD013 at 99 m. (f) Scheelite mineralisation (Sch) affected by the S_{1-2} fabric (few white traced lines for reference) in D_{1-2} monzonite (drill core MWD013 at 99 m) under UV light. (e) shows the same sample without UV light. (g) Granitic East dyke. (h) Skarn-altered conglomerate (drill core MWD011 at 147.5 m) under UV light showing D_{1-2} sigmoidal scheelite (Sch) mineralisation along ductile S_{1-2} fabric. (i) Detailed images of a multi-stage scheelite-rich quartz–plagioclase syn-D_4 vein from drill core MWD107 at 259 m (note the blue colour of scheelite under UV light in the bottom image). The letters in the image denotes different stages within the veins: (I) early plagioclase + scheelite (Sch + Pl)–quartz (Qz) assemblage as margins of veins (retrograde stages 1 and 2; Figure 5); (II) grey quartz, (III) white quartz veinlets, (IV) calcite stringers from retrograde stage 3, and (V) late pyrrhotite fracture filling from the late retrograde stage 4. Note the relationship between the centimetric dark vein halo and the skarn-altered conglomerate on the top image.

syn-D_{1-2}, Ca-rich garnet (Grs_{40-65}), actinolite, and plagioclase (Figure 5). The D_{1-2} quartz, plagioclase, actinolite and garnet assemblage formed during peak metamorphism (Poblete *et al.*, 2021).

Syn-D_4 scheelite mineralisation associated with veining

The bulk of economic scheelite mineralisation at Watershed is hosted by veins associated with D_4 shear zones, and disseminations in vein haloes within skarn-altered conglomerate, where scheelite is intergrown with clinozoisite (Poblete *et al.*, 2021; Figures 4i and 5). The veins are of limited length (<30 m), vary in width from a few centimetres to 3 m and terminate abruptly in slate and/or slate–siltstone breccia. The widest veins are extensional in nature and generally trend east with a steep southerly dip (Figure 3a). Veins in all other orientations are thinner (<10 cm; Poblete *et al.*, 2021).

The D_4 veins opened in several stages (Poblete *et al.*, 2021). The margins of the D_4 veins contain feldspar, scheelite and

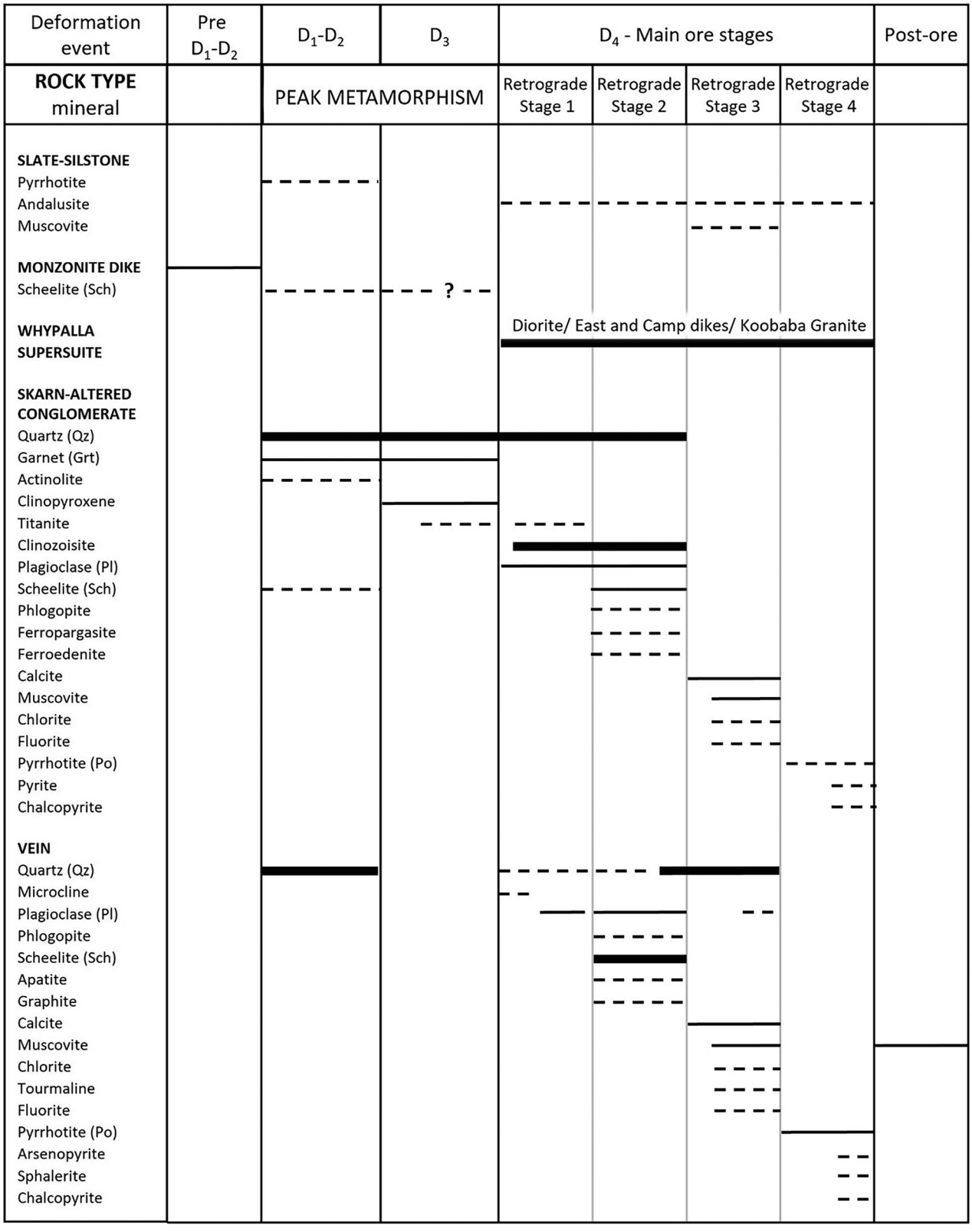

Figure 5. Mineral paragenesis of the Watershed tungsten deposit.

quartz (Figure 4i), which represent retrograde stages 1 and 2 (Figure 5). During retrograde stage 1, early sanidine (overgrown by plagioclase, $An_{15–55}$) formed with minor quartz in the vein margin (Poblete *et al*., 2021). Retrograde stage 2 is represented by intergrown scheelite (containing graphite inclusions; Figure 6d; supplemental data, Table S2) and plagioclase ($An_{3–43}$) that overgrow earlier plagioclase, phlogopite and trace apatite (Poblete *et al*., 2021). Further vein opening

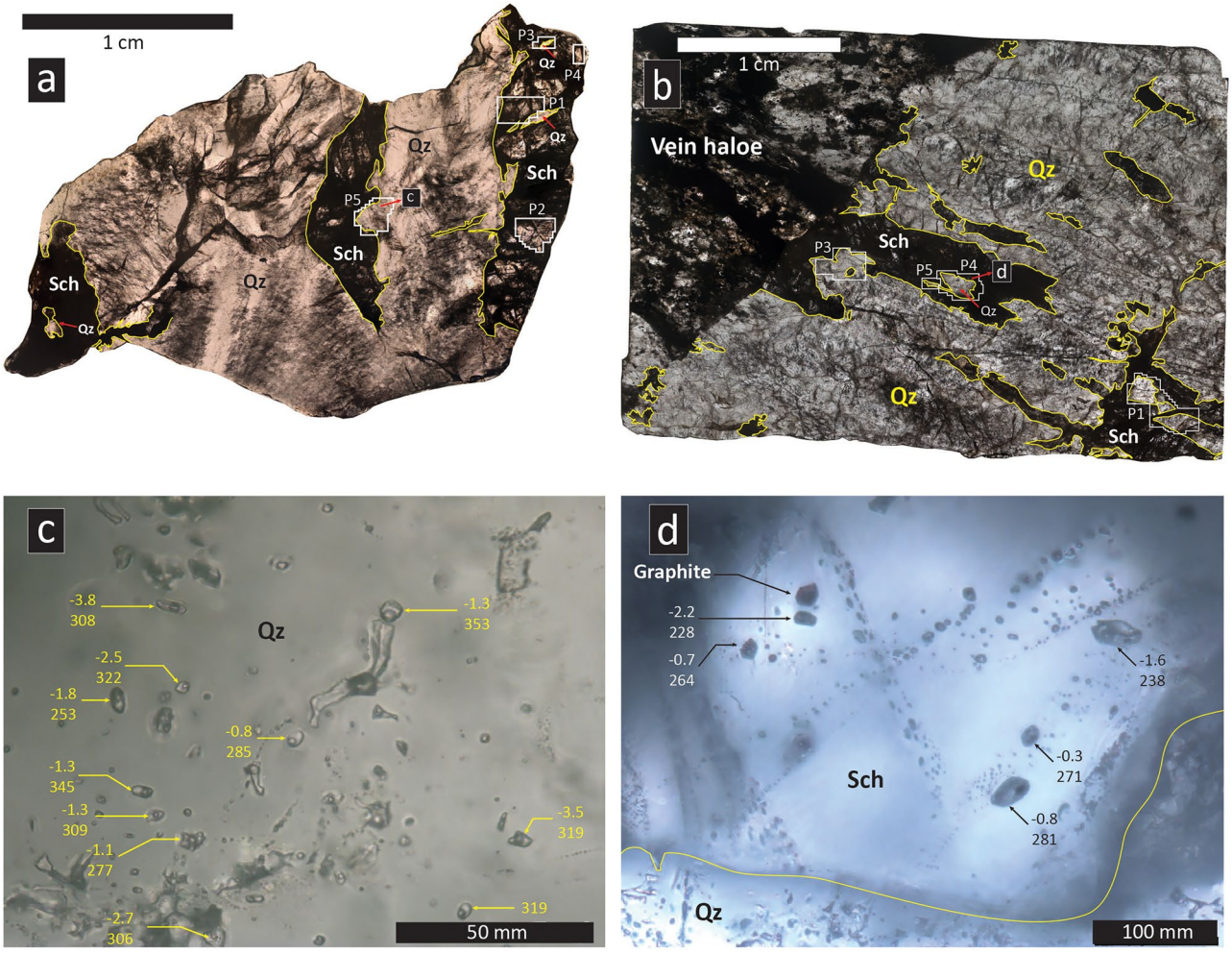

Figure 6. Microphotographs of analysed samples for fluid inclusions. For sample locations see Figure 3a, b. Mineral abbreviations are from Whitney and Evans (2010). (a) Stitched image of sample MWD099-054B where scheelite (Sch) is cut and intergrown with quartz (Qz). Yellow contours denote scheelite (Sch) margins. Analysed areas (P1 to P5) are shown. (b) Stitched image of sample MWD099-124B where scheelite (Sch) is growing perpendicular to vein wall in a pure tension regime. Scheelite is intergrown and crosscut by quartz (Qz). Yellow contours denote scheelite (Sch) margins. Analysed areas (P1, P3 to P5) are shown. (c) Stitched microphotographs from different focus levels of a quartz grain from FIA#20 (in area P5-7; Figure 5a; supplemental data, Table S2) from sample MWD099-054B. Final ice-melting temperature (T_m) and homogenisation temperatures (T_h) are indicated in °C. (d) Stitched microphotographs from different focus levels of a scheelite (Sch) grain from FIA#44 (P4-1; Figure 5b; supplemental data, Table S2) from sample MWD099-124B. Final ice-melting temperature (T_m) and homogenisation temperatures (T_h) are indicated in °C. Note the graphite inclusion within scheelite (Sch).

during retrograde stage 3 resulted in the infill of the central part of the vein by grey and white quartz, which was subsequently cut across by muscovite and calcite (Figure 4i) with minor chlorite, tourmaline and fluorite. Retrograde stage 4 fractures cut the previous stages and contain pyrrhotite (Figure 4i) and arsenopyrite, with lesser pyrite, chalcopyrite and sphalerite (Figure 5).

Sample selection

Fluid-inclusion samples

Fluid-inclusion studies were carried out on two drill-core samples (MWD099-054B and MWD099-124B; Figure 3a; supplemental data, Table S1) with coexisting scheelite and quartz (occurring as inclusions in scheelite), which formed during retrograde stage 2 in mineralised D_4 veins (Figures 5 and 6a, b).

Isotope samples

Oxygen ($\delta^{18}O$) isotope data were collected from D_4 scheelite, plagioclase, quartz, and muscovite grains (Figure 3; supplemental data, Table S1) in veins and vein haloes associated with the different retrograde stages of mineralisation. Scheelite, plagioclase and quartz were collected from veins associated with the retrograde stage 2 (Figure 5). Muscovite was collected from a vein halo (WS16-006; Figure 2) near a mineralised D_4 vein, and from the muscovite centrelines in D_4 veins from drill-core associated with retrograde stage 3 (Figures 3a and 5). The vein centrelines formed during a later, post-ore event (Figure 5) associated with the Hunter–Bowen Orogeny (Henderson *et al.*, 2013; Poblete *et al.*, 2021). Sulfur isotopic values ($\delta^{34}S$) were measured on retrograde stage 4 pyrrhotite, arsenopyrite, pyrite and sphalerite in D_4 veins (Figures 3a and 5; Table 4; supplemental data, Table S1). The

δD isotopic data were collected from muscovite in a D_4 vein-halo, and from muscovite centrelines in D_4 veins (Figures 3a and 5; Table 3; supplemental data, Table S1).

Analytical techniques

Microthermometry

Twenty-four samples were inspected to assess their suitability for fluid inclusion studies. Of those, two samples were selected for detailed study. Doubly polished sections (~200 µm thick) were used for microthermometry measurements at James Cook University, Townsville, Australia. Fluid inclusion microthermometry was conducted using a Linkham MDS600 heating-freezing stage (temperature range between −196 and +600 °C), attached to an Olympus BX51 microscope with 40× and 50×, long-working distance objectives. The MDS600 heating-freezing stage was operated with the Linksys 32 software. Samples were placed within the insulated stage on a 10 mm-diameter quartz lens. Pure CO_2 and H_2O inclusions in quartz (supplied by FluidInc) were used for regular calibration at the triple points of CO_2 (−56.6 °C) and H_2O (0.0 °C). Critical homogenisation temperatures of synthetic H_2O inclusions in quartz were used for calibration at 374 °C. Phase transitions below room temperature have a precision of ±0.3 °C; and homogenisation measurements of aqueous inclusions have a precision of ±5 °C. The following phase transitions were systematically measured during the freezing and heating experiments. (1) Metastable freezing temperatures of the liquid phase in aqueous fluid inclusions. The metastable freezing temperature is not an exact indicator of the salinity of the aqueous phase but does provide a good indication of the final ice-melting temperatures (Wilkinson, 2017). (2) Initial melting of ice in aqueous fluid inclusions. (3) Final melting of ice in aqueous fluid inclusions. (4) Homogenisation of aqueous fluid inclusions. (5) Clathrate melting, only observed in larger fluid inclusions. The density and salinity of aqueous fluid inclusions were calculated using the software HokieFlincs (Steele-MacInnis *et al*., 2012).

Raman microspectroscopy

Laser Raman microspectroscopy analyses were carried out using a WITec Alpha300 Access Raman micro-spectrometer at the Advanced Analytical Centre of James Cook University, Townsville, Australia. The WITec Alpha300 Access is equipped with a 532.1 nm UHTS 300 SMFC VIS-NIR laser source. Data processing was done with the WITec Project Data Analysis Software 4.1. The database compiled by Frezzotti *et al*. (2012) was used to identify the fluid composition and solid phases.

Stable isotope analyses

Oxygen isotope values for plagioclase, quartz, muscovite and scheelite were analysed at the Stable Isotope Laboratory at GNS Science (New Zealand). Oxygen was extracted from silicate and scheelite sample powders for isotope analyses using a CO_2 laser and BrF_5 (Sharp, 1990). Oxygen isotope values have been reported using the $\delta^{18}O$ notation, relative to Vienna Standard Mean Ocean Water (VSMOW). Samples were normalised to the international quartz standard NBS-28 using a value of +9.6 per mil (‰). Results for four NBS-28 analyses measured together with the samples had values that varied <0.15‰. Samples and standards were heated overnight to 200 °C prior to being loaded into the vacuum extraction line and were then evacuated for approximately 6 hours. Blank BrF_5 runs were done until the yield was <0.2 µmol of oxygen. Oxygen yields were recorded, and CO_2 gas was analysed on a Geo 20-20 mass spectrometer. Muscovite hydrogen isotope samples were analysed on a HEKAtech, high-temperature elemental analyser coupled to a GV Instruments IsoPrime mass spectrometer. Samples were pyrolysed at 1450 °C in silver capsules, and all samples were analysed in triplicate. All results have been reported relative to VSMOW, normalised to international standards IAEA-CH-7, NBS30 and NBS22 (with reported values of −100, −66 and −118‰, respectively) and waters USGS46, 47, 48 and W62001 (with reported values of −235.8, −150.2, −2.0 and −41.1‰, respectively). The external precision for these measurements is better than 2‰.

Sulfur ($\delta^{34}S$) isotope analyses for sulfide mineral phases were performed at the Central Science Laboratory of the University of Tasmania, Hobart, Australia using an NCS Combustion Mode coupled with an IsoPrime100 IRMS (stable isotope ratio mass spectrometry) detector. Sulfide samples were drilled directly from the rock (10 mg), after which a small amount of powdered material (0.1 mg sulfur) was used for each analysis. Sulfides were combusted at a temperature of 1150 °C in an O_2-enriched He atmosphere. After combustion, the bulk sample gas was stripped of H_2O in water traps, and of SO_2 and CO_2 in the 'purge and traps' columns. The N_2 component gas is not trapped in a column and is the first to enter the IRMS. The final gas to be released is SO_2, which occurs when the desorption column is heated to 220 °C. The sample gas subsequently bypasses the CO_2 column, passes through a second water trap and enters the IRMS. Reference He, N_2, CO_2 and SO_2 are injected into the IsoPrime100 IRMS prior to each of the unknown measured components. The international reference standards and internal standards were repeatedly measured between samples to control analytical reproducibility. The precision was 0.2‰ for $\delta^{34}S$ and 0.25% for sulfur-elemental analysis. All sulfur isotope values have been expressed as a delta notation in per mil (‰) relative to Cañón Diablo Troilite (CDT; Ault, 1963).

Fluid inclusion results

Fluid inclusions in quartz

Fluid-inclusion assemblages (FIAs) in quartz coexisting with scheelite include FIAs defined by clustered primary fluid inclusions, FIAs defined by short trailbound fluid inclusions that do not crosscut the grain boundary and interpreted to be pseudo-secondary, and late FIAs defined by trailbound fluid inclusions that do crosscut the grain boundaries and interpreted to be secondary. The late trail FIAs were excluded from this study

because they postdate the mineralisation event. The FIAs defined by clustered fluid inclusions comprise irregularly shaped fluid inclusions (4–90 µm in size) that contain an aqueous liquid phase and a bubble (Figure 6c). The bubble volume varies between 4 and 38 vol%. Raman microspectroscopy showed that within individual FIAs, the bubbles of some of the fluid inclusions contained CH_4 (Figure 7a, c). Methane was also detected in the aqueous liquid phase (supplemental data, Table S2) in some of those fluid inclusions that contain a CH_4 bubble. Some of the CH_4-bearing fluid inclusions contain graphite as identified by Raman microspectroscopy (Figure 7). In a few larger fluid inclusions, the presence of CH_4 was confirmed by clathrate melting between +1 and +16 °C.

Importantly, no liquid–vapour phase separation was observed inside the CH_4 bubble during cooling to temperatures of −120 °C, which indicates that the bubble comprises a CH_4 vapour phase with a maximum density of 0.019 g/cm^3 (*i.e.* a molar volume >840 cm^3/mol) and is the density of a CH_4-fluid phase homogenising to the vapour phase at −120 °C (Setzmann & Wagner, 1991). The maximum density of 0.019 g/cm^3 and the

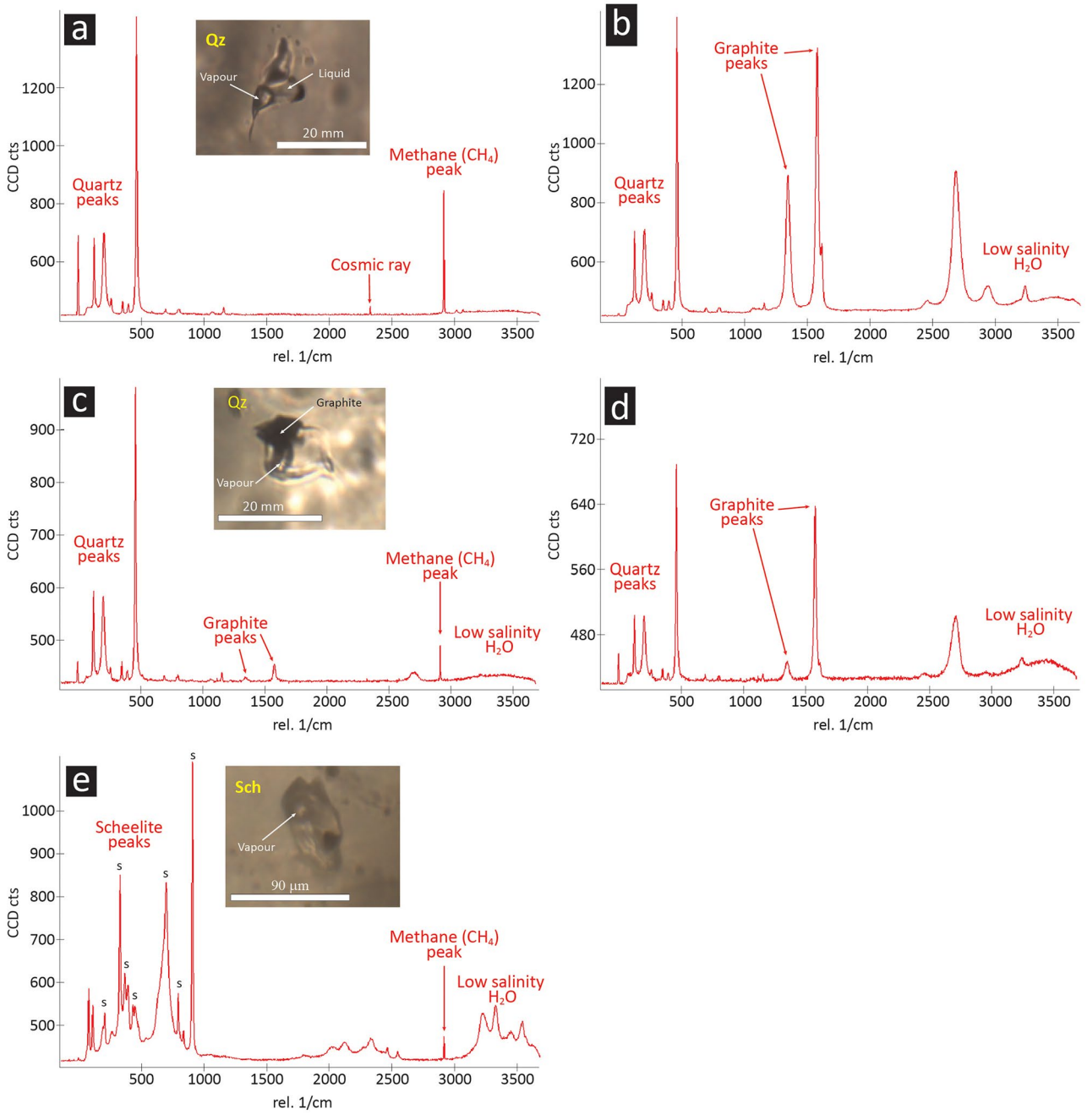

Figure 7. Example of Raman microspectroscopy analysis of fluid inclusions in quartz and scheelite in sample MWD099-124B (supplemental data, Table S2). (a) Vapour phase in fluid inclusion P4-2-3 from FIA#37 in quartz (Figure 5b). Inset microphotograph shows fluid inclusion. (b) Liquid phase in fluid inclusion P4-2-3 from FIA#37 in quartz (Figure 5b). (c) Vapour phase in fluid inclusion P1-1-1 from FIA#22 in quartz (Figure 5b). Inset microphotograph shows fluid inclusion. (d) Solid phase in fluid inclusion P1-1-1 in quartz (Figure 5b). (e) Vapour phase in fluid inclusion P4-1-2 from FIA#44 in scheelite (Figure 5b, d). Inset microphotograph shows fluid inclusion. Mineral abbreviations are from Whitney and Evans (2010).

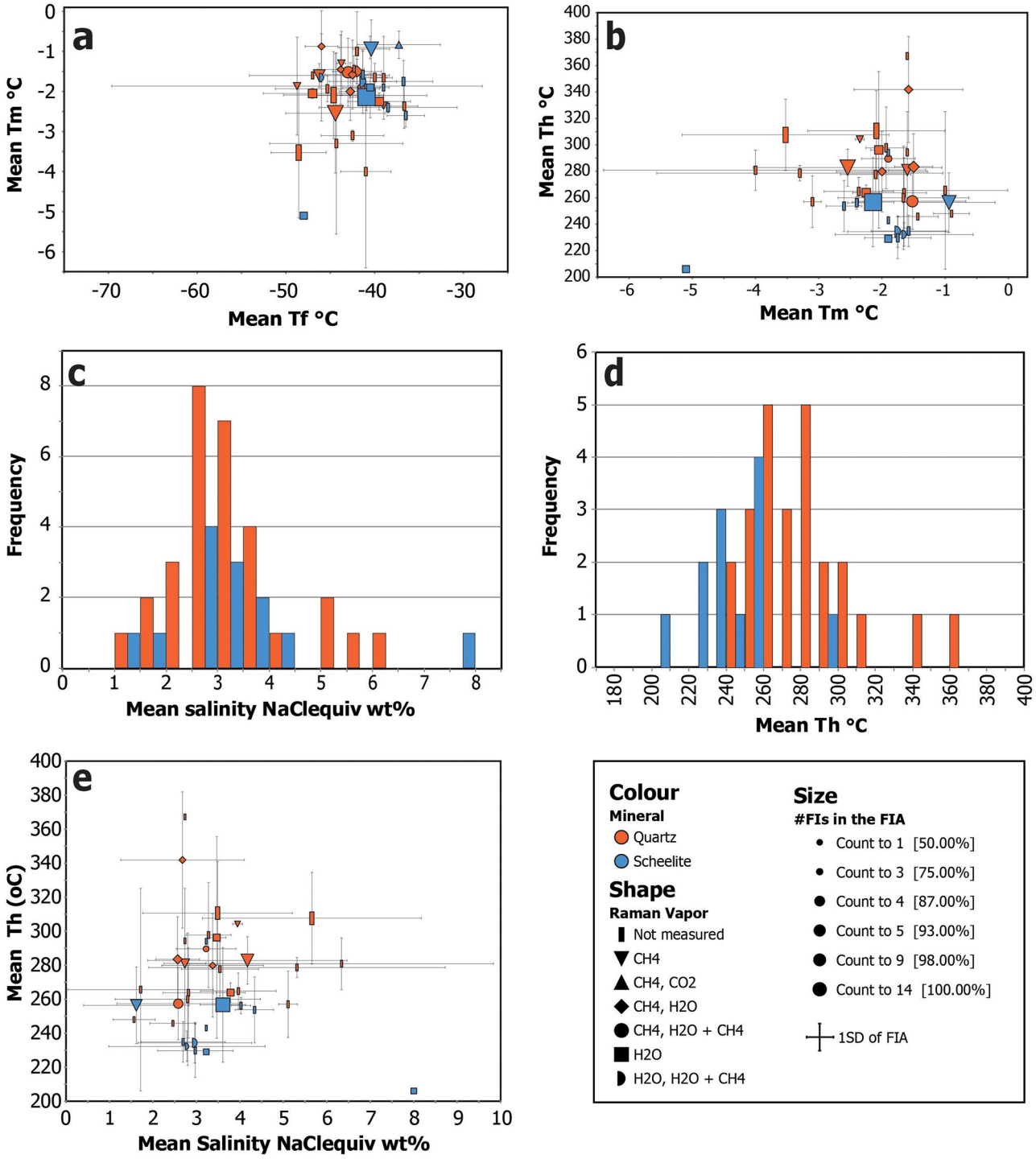

Figure 8. Selected FIAs graphs from Watershed from this work. Full data set in supplemental data, Table S2. (a) Metastable freezing temperature (T_f) *vs* final ice-melting temperatures (T_m). (b) Final ice-melting temperature (T_m) *vs* homogenisation temperature (T_h). (c) Frequency distribution for salinity. (d) Frequency distribution for homogenisation temperature (T_h). (e) Salinity ($NaCl_{eq}$) *vs* homogenisation temperature (T_h).

Table 1. Characteristics of the measured fluid inclusions.

Mineral	D_4 quartz	D_4 scheelite
Composition	H_2O–NaCl–CH_4 H_2O–NaCl (3.3 ± 1.6 wt% $NaCl_{eq}$)	H_2O–NaCl–CH_4 H_2O–NaCl (3.5 ± 0.9 wt% $NaCl_{eq}$)
Density [g/cm^3] (average)	0.67–0.86 (0.79 ± 0.05)	0.76–0.84 (0.80 ± 0.04)
Fluid source	Metamorphic ± igneous	Metamorphic ± igneous

volume of the CH_4 vapour phase (10–30 vol%) constrain the CH_4 content of the fluid inclusions with a CH_4 vapour bubble to a maximum of 1 mol% (*i.e.* 0.6 mol/kg), but it must be noted that the exact composition cannot be determined.

Microthermometric results

The specific microthermometric results of fluid inclusions containing CH_4 are not presented here, as we cannot determine the

precise composition of these fluid inclusions, hindering further interpretation. Consequently, we only report the microthermometric results of the H_2O–NaCl fluid inclusions of which we are sure that they do not contain CH_4 (*e.g.,* FIA 13 and FIA 14; supplemental data, Table S2). Initial melting of the frozen aqueous phase occurred between −31 and −22 °C, corresponding to the (meta-)stable, eutectic melting temperature of the H_2O–NaCl system (Goldstein & Reynolds, 1994). Final ice melting occurred at temperatures of between −2.4 and −1.9 °C (Figure 8a–c) indicating a low salinity of 3.2–4.0 wt% $NaCl_{eq}$, which is in good agreement with the freezing temperatures of the aqueous liquid phase between −52 and −37 °C (Figure 8a; Wilkinson, 2017). Homogenisation into the liquid phase occurred between 228 and 337 °C (Figure 8b, d) indicating a density range of 0.67–0.83 g/cm^3 (Table 1).

Fluid inclusions in scheelite

FIAs in scheelite are identical to those in quartz in both appearance and composition (Table 1). They include FIAs defined by clustered fluid inclusions and by short trailbound fluid inclusions that do not crosscut the grain boundary. The size of the irregular and regular-shaped fluid inclusions in the FIAs varies between 5 and 44 µm (Figure 6d). The fluid inclusions contain an aqueous liquid phase and a bubble. Similar to the fluid inclusions in quartz, the bubble size varies from 4 to 33 vol%. Also, like in quartz, CH_4 was detected by Raman microspectrometry in the bubble of some fluid inclusions as a vapour phase (<1 mol% CH_4; Figure 7e; supplemental data, Table S2). Graphite was detected in only one CH_4-bearing fluid inclusion by Raman microspectroscopy. Again, like for the fluid inclusions hosted in quartz, it must be noted that the exact composition of the CH_4-bearing fluid inclusions cannot be determined.

Microthermometric results

As for quartz, microthermometric results of CH_4-bearing fluid inclusions are not presented here, and we only report the microthermometric results of the H_2O–NaCl fluid inclusions combining the data of all FIAs in scheelite (*e.g.,* FIA 3, FIA 4 and FIA 7). Initial melting of the frozen aqueous phase was observed between −32 and −22 °C indicating the presence of NaCl, similar to the FIAs in quartz. Final melting of ice occurred between −5.1 and −1.6 °C indicating a salinity range of 2.7–8.0 wt% $NaCl_{eq}$ (Figure 8a–c; supplemental data, Table S2), which agrees with the freezing temperatures of the aqueous liquid phase of between −48 and −38 °C (Figure 8a). Homogenisation into the liquid phase was observed at temperatures that varied between 206 and 333 °C (Figure 8b, d) indicating a density range of 0.68–0.92 g/cm^3 (Table 1). Clathrate melting was observed for a few larger fluid inclusions at temperatures of between +4 and +17 °C.

Stable isotope results

Scheelite, quartz and plagioclase

Scheelite grains hosted in D_4 veins (retrograde stage 2; Figure 5) yield $\delta^{18}O_{VSMOW}$ values of +3.8 to +7.3‰ (n = 17) with an average value of +5.4 ± 1.1‰ (Table 2). Plagioclase grains coexisting with scheelite (Figure 5) yield $\delta^{18}O_{VSMOW}$ values of +7.0 to +11.8‰ with an average value of +10.3 ± 1.4‰ (*n* = 14; Table 2). Quartz that formed with or slightly postdated the growth of

Table 2. Oxygen isotope data of scheelite and silicates from different rock types and deformation events.

Sample no.	Deformation rock type	$\delta^{18}O$ (‰) Scheelite	$\delta^{18}O$ (‰) Plagioclase	$\delta^{18}O$ (‰) Quartz	Δsch–ab^{18}O[a]	*T* °C albite	$\delta^{18}O_{H2O}$ (‰)	Δsch–qz^{18}O[b]	*T* °C Quartz	$\delta^{18}O_{H2O}$ (‰)
MWD036-075.5	D_4 vein	+4.1	+11.2	+13.7	7.2	234	+4.6	9.6	254	+10.8
MWD042-197	D_4 vein	+5.7		+12.8				7.1	385	
MWD077-145	D_4 vein	+5.2	+11.8	+14.2	6.6	260	+6.2	9.1	276	+11.4
MWD099-054	D_4 vein	+3.7	+9.4		5.6	339	+5.9			
MWD099-163.5	D_4 vein	+7.2	+11.6	+13.2				6.0	473	+10.4
MWD101-149	D_4 vein	+7.3		+13.5						
MWD101-155	D_4 vein	+5.2	+10.4		5.2	409	+8.1			
MWD101-159	D_4 vein	+6.3	+9.7							
MWD105-077	D_4 vein	+5.1	+11.7	+13.7	6.6	265	+6.2	8.5	300	+10.8
MWD105-123.5	D_4 vein	+4.8	+10.9	+15.5	6.2	293	+6.3	10.7	219	+12.6
MWD105-135	D_4 vein	+6.7	+11.2	+13.9				7.3	370	+11.0
MWD105-206	D_4 vein	+4.8	+8.8							
MWD107-259	D_4 vein	+6.1	+11.5	+14.7	5.4	366	+8.6	8.6	295	+11.8
MWD124-240	D_4 vein	+6.0		+12.6				6.6	419	+9.7
MWD194-105.5	D_4 vein	+3.8	+10.1	+14.8	6.3	279	+5.1	11.0	208	+11.9
MWD217-078	D_4 vein	+5.6	+7.0	+14.8				9.2	271	+11.9
MWD217-189.5	D_4 vein	+4.4	+8.8	+15.1				10.7	218	+12.2
	Minimum				5.2	234	+4.6	6.0	208	+9.7
	Maximum				7.2	409	+8.6	11.0	473	+12.6
	Average				6.1	306	+6.4	8.7	307	+11.3
	Standard deviation				0.6	56	+1.3	1.6	82	+0.8

[a]Albite – H_2O; °C (Zheng, 1993a); scheelite – H_2O; 100–500 °C (Wesolowski & Ohmoto, 1986).
[b]Quartz (alpha) – H_2O; 200–500 °C (Clayton *et al.*, 1972); scheelite – H_2O; 100–500 °C (Wesolowski & Ohmoto, 1986).

Table 3. Oxygen and hydrogen isotope data of muscovite.

Sample No.	Location	δD (‰) VSMOW	$\delta^{18}O$ (‰) VSMOW
MWD217-133A	Vein centreline	−73.4	11.5
MWD217-149A	Vein centreline	−68.7	12.4
WS16-006	Vein halo	−63.3	13.2

Table 4. Sulfur isotope data for D_4 sulfide minerals.

Mineral	Sample no.	$\delta^{34}S$‰ CDT
Arsenopyrite	MWD124-193.5B	−0.2
	MWD217-133A	+1.3
	MWD217-048.5A	+1.4
	MWD231-043A	+1.9
	MWD217-078A	+2.8
Pyrite	MWD217-142A	−0.5
	MWD101-149A	−0.4
	MWD101-119A	+1.3
Pyrrhotite	MWD105-206A	−2.5
	MWD105-215A	−2.2
	MWD107-062.5A	−1.7
	MWD124-180A	−1.5
	MWD217-181A	−1.3
	MWD124-280.5B	−1.2
	MWD101-222A	−0.9
	MWD124-193.5A	−0.9
	MWD105-234A	−0.8
	MWD231-068A	−0.7
	MWD124-130.5A	−0.5
	MWD042-269B	+0.2
	MWD101-211.5A	+0.2
	MWD194-105.5A	+0.5
	MWD101-104A	+0.8
	MWD101-121.5A	+1.1
	MWD105-200A	+2.2
Sphalerite	MWD194-065A	−0.2
	MWD217-056A	+0.3

scheelite and plagioclase (Figure 5) yields $\delta^{18}O_{VSMOW}$ values that range from +12.6 to +15.5‰ ($n = 13$) with an average value of +14.0 ± 0.9‰ (Table 2).

Muscovite

Three retrograde stage 3 muscovite samples from D_4 veins, two samples from a muscovite centreline and one muscovite grain from the vein halo were analysed for oxygen ($\delta^{18}O_{VSMOW}$) and hydrogen (δD_{VSMOW}) isotopes. The $\delta^{18}O_{VSMOW}$ values for muscovite along the centrelines are +11.5 and +12.4‰. The $\delta^{18}O_{VSMOW}$ value for muscovite from the vein halo is +13.2‰. The δD_{VSMOW} values for the centreline muscovite grains are −73.4 and −62.7‰. The δD_{VSMOW} value for muscovite from the vein halo is −63.3‰ (Table 3).

Sulfides

Sulfur isotope data ($\delta^{34}S_{CDT}$) for pyrrhotite ($n = 17$), arsenopyrite ($n = 5$), pyrite ($n = 3$) and sphalerite ($n = 2$) in D_4 veins from retrograde stage 4 are presented in Table 4. $\delta^{34}S_{CDT}$ values for all sulfide minerals fall within a narrow range of −2.5 to +2.8‰, with an average value of −0.06 ± 1.31‰. Pyrrhotite showed the largest spread (ranging from −2.5 to +2.2‰ with an average value of −0.54 ± 1.19‰), and arsenopyrite yielded the highest values (ranging from −0.12 to +2.8‰ with an average value of +1.44 ± 0.97‰). Pyrite and sphalerite grains yield values that ranged from −0.5 to +1.3‰ (average at +0.10 ± 0.83‰) and −0.23 to +0.3‰ (two measurements only), respectively (Figure 9a).

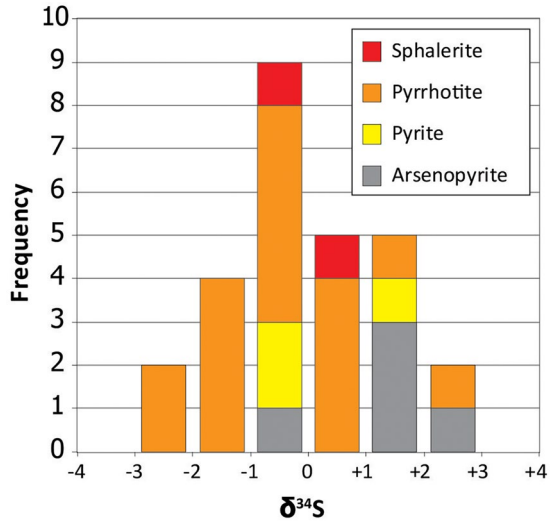

Figure 9. Frequency distribution showing the $\delta^{34}S_{CDT}$ values for sulfides from the retrograde stage 4 (sulfide stage) at Watershed.

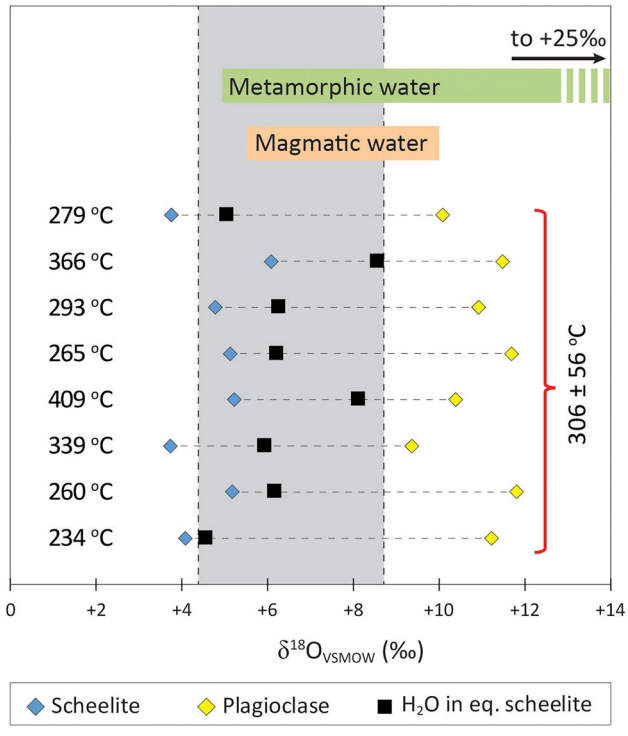

Figure 10. Oxygen isotopic composition for scheelite, plagioclase and water in equilibrium with the scheelite and plagioclase in D_4 veins. The fluid $\delta^{18}O_{VSMOW}$ compositions overlap with an igneous and a metamorphic fluid origin (Taylor, 1974). Also shown are the temperatures calculated using scheelite–plagioclase oxygen isotope fractionation (Table 2).

Discussion

Fluid composition

Primary fluid inclusions in coexisting scheelite and quartz are identical in composition (Figure 8a, b; Table 1), with low to medium salinities (0.2–8.0 wt% $NaCl_{eq}$). The observed salinities are similar to other scheelite-dominated deposits (Goldfarb *et al*., 2005; Wood & Samson, 2000). The similarity in composition for fluid inclusions found in scheelite and quartz implies crystallisation from the same fluid, as to be expected considering the coexistence of quartz and scheelite (Figure 5). The presence of CH_4-bearing aqueous fluid inclusions and aqueous fluid inclusions without CH_4 within the same FIA indicates heterogeneous trapping of a H_2O–NaCl and a CH_4-bearing fluid phase (*e.g.,* Hurai, 2010; Ramboz *et al*., 1982). The presence of graphite in only some of the CH_4-bearing fluid inclusions (Figures 6 and 7b–d) suggests that graphite was present at the time of fluid trapping. The absence of graphite in some of the CH_4-bearing fluid inclusions can be explained by the absence of graphite nucleation (Ramboz *et al*., 1985). The fluid inclusions show a significant spread in salinities (Figure 8), which can be explained by fluid–fluid mixing (Wilkinson, 2001) indicating the presence of at least two fluid sources during mineralisation (see below).

Temperature and pressure of mineralisation

To determine the mineralisation temperatures, we used the oxygen isotope pair of scheelite and plagioclase, and the fractionation equations of Wesolowski and Ohmoto (1986) and Zheng (1993a). The calculated temperatures are between 234 and 409 °C, with an average of 306 ± 56 °C (1SD; Figure 10; Table 2). These temperatures are statistically indistinguishable from the 307 ± 82 °C temperatures (208–473 °C total range), obtained from the scheelite and quartz oxygen isotope pairs (using the fractionation equation of Wesolowski & Ohmoto, 1986). These data agree with the petrography showing that scheelite coexists with some of the quartz.

To determine the mineralisation pressure under which the H_2O–NaCl FIAs were formed, we used the mineralisation temperatures and the isochores for the H_2O–NaCl fluid inclusions (*e.g.,* Roedder & Bodnar, 1980). The isochores were calculated following Bodnar and Vityk (1994). An FIA composition of 3.9 wt% $NaCl_{eq}$ (*i.e.,* final ice-melting temperature > −2 °C; see Figure 8b, c) was considered to calculate the isochores. The isochores were calculated for the first (238 °C) and third (281 °C) quartile of the homogenisation temperatures of the primary H_2O–NaCl FIAs in scheelite (Figure 8d).

Using the formation temperature range of 306 ± 56 °C obtained from the scheelite–plagioclase oxygen isotope

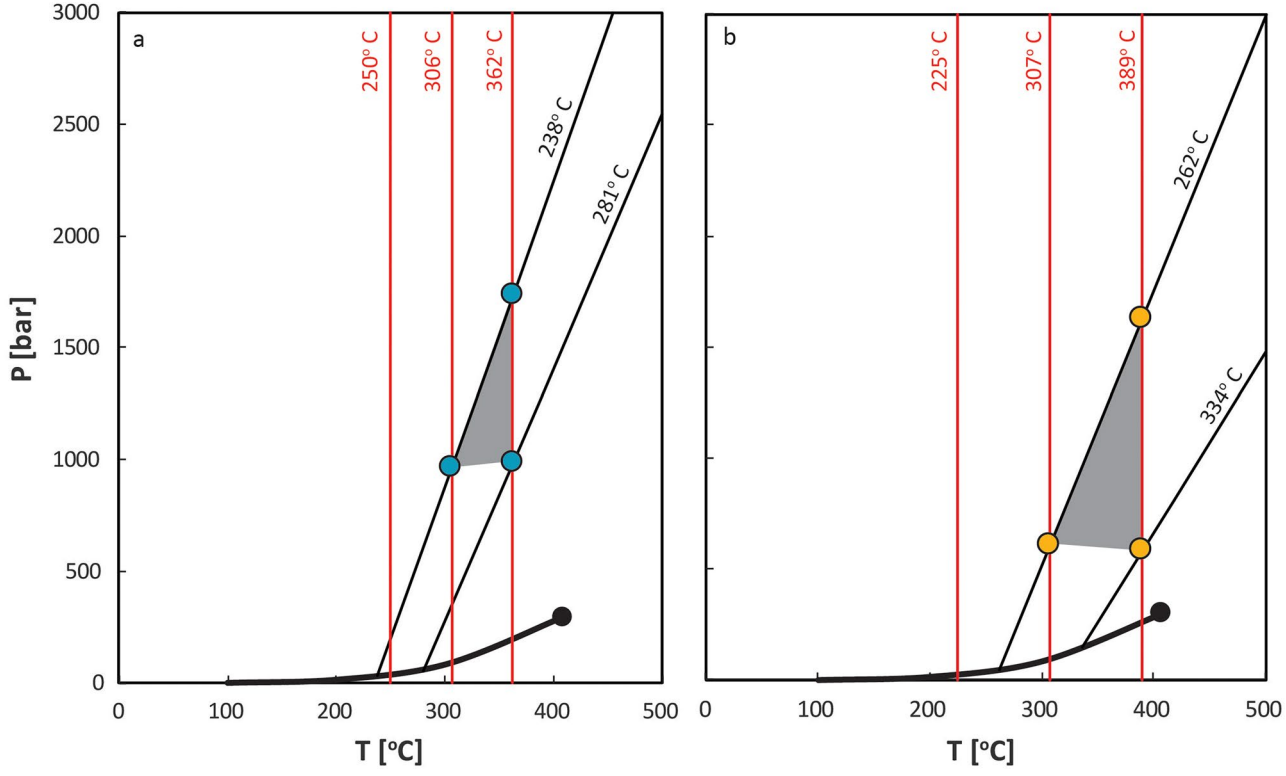

Figure 11. *P–T* diagrams for the H_2O–NaCl system where the grey areas represent the (a) scheelite and (b) quartz mineralisation pressure–temperature conditions, calculated using Hokieflincs (Steele-MacInnis *et al*., 2012). (a) Scheelite diagram considering 3.87 wt% $NaCl_{eq}$ where the black lines show the isochores for the first (238 °C) and third (281 °C) quartiles for the homogenisation temperatures measured in H_2O–NaCl fluid inclusion assemblages (FIAs 3, 4 and 7). The red lines represent the independent temperature constraints calculated using the oxygen fractionation between scheelite and plagioclase (306 ± 56 °C; Wesolowski & Ohmoto, 1986; Zheng, 1993a). (b) Quartz diagram considering 3.55 wt% $NaCl_{eq}$ where the black lines represent the isochores for the first (262 °C) and third (334 °C) quartiles for the homogenisation temperatures measured H_2O–NaCl fluid inclusion assemblages in quartz (FIAs 13 and 14). The red lines are the independent temperature constraints calculated using oxygen fractionation between quartz and scheelite (307 ± 82 °C; Clayton *et al*., 1972; Wesolowski & Ohmoto, 1986).

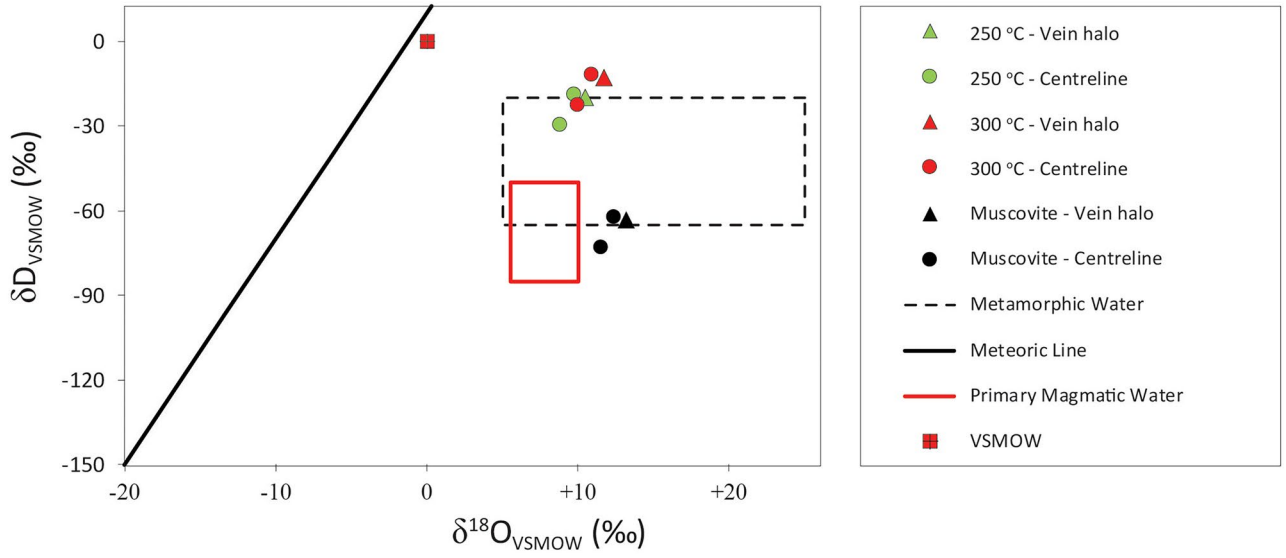

Figure 12. Muscovite δD and $\delta^{18}O_{VSMOW}$ isotopic values from muscovite at different temperatures at Watershed show a metamorphic origin for the muscovite formation. Black symbols are the isotopic composition of muscovite at Watershed. The magmatic and metamorphic water fields are from Taylor (1974), the meteoric line is from Craig (1961).

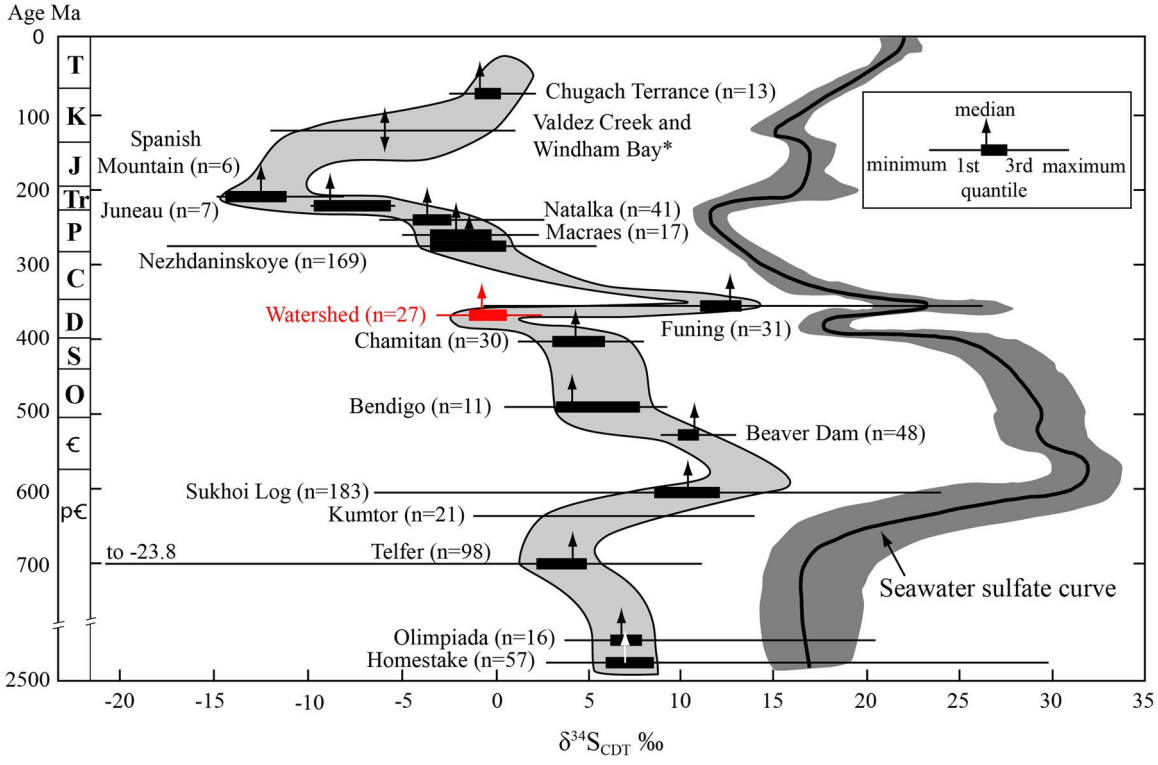

Figure 13. Historical distribution of $\delta^{34}S_{CDT}$ for sediment hosted orogenic gold deposits compared with the historical $\delta^{34}S_{CDT}$ of seawater sulfate (modified after Chang *et al.*, 2008). Sulfur isotope data from Watershed (shown in red) falls in this trend implying that the sulfur that formed the sulfide minerals at Watershed during D_4 originated from the reduction of seawater sulfate.

thermometer together with the calculated isochores, the mineralisation pressure can be constrained to 1–1.8 kbar for 3.9 wt% $NaCl_{eq}$ in scheelite and 3.6 wt% $NaCl_{eq}$ in quartz (Figure 11a, b). Assuming a lithostatic fluid pressure and an average density of 2700 kg/m^3, these results indicate a depth of mineralisation of 3.7–6.7 km and a corresponding elevated geothermal gradient of between 35 and 75 °C/km. Similarly with quartz, we use the formation temperature range of 307 ± 82 °C obtained from the scheelite–quartz oxygen isotope thermometer, and the first and third quartile values of 262 and 334 °C for the homogenisation temperatures of primary FIAs in quartz (Figure 8d) to calculate the pressures. The results show that the quartz precipitated at a pressure of 0.6–1.7 kbar (Figure 11c, d), similar to the formation pressures of scheelite.

The *P–T* conditions of the D_4-vein scheelite are similar to those of lode-gold deposits (Goldfarb & Groves, 2015), including the Hodgkinson Gold Field (Figure 1b) to the south of Watershed (Peters *et al*., 1990; Vos & Bierlein, 2006), where mineralisation occurred at *P–T* conditions of <1.5 kbar and 150–400 °C, respectively. These *P–T* conditions indicate a high geothermal gradient (35–145 °C/km), which can be explained as a result of Permian magmatism (Figure 1b). The heat released from the Permian intrusions increased the fluid temperatures, which may have enhanced the flow of the metamorphic fluids, and the metal solubility and transportation.

Redox conditions during mineralisation

Redox conditions of mineralisation at Watershed can be determined from the mineral phases that accompanied scheelite mineralisation. At Watershed, the mineralogy in skarn-altered conglomerate is characterised by garnet with a low andradite content, clinozoisite rather than epidote, and pyrrhotite and arsenopyrite in D_4 veins (Poblete *et al*., 2021; Figure 5). This is indicative of reduced conditions, which is confirmed by the presence of CH_4 and graphite in some of the fluid inclusions (Figure 7a, c, e), plus the graphite inclusions in quartz and scheelite (Figure 6d). These findings agree with the reduced conditions described for some tungsten skarn deposits (Kwak, 1987; Shimazaki, 1980).

Source of fluids

The origin of the mineralising fluids can be constrained from isotope data for different mineral phases in D_4 veins. The $\delta^{18}O_{water}$ values can be calculated using the isotope fractionation equations for the scheelite–water system (Wesolowski & Ohmoto, 1986) and the formation temperatures between 234 and 409 °C obtained from scheelite–plagioclase O-isotope pairs (Table 2). The obtained values for the D_4 fluid range from +4.6 to +8.6‰. The values are inconclusive; they can be explained by either a magmatic or a metamorphic source for the fluid, or a combined magmatic–metamorphic fluid (Taylor, 1974; Figure 10).

In a similar manner, the $\delta^{18}O_{water}$ values of the fluid involved in the formation of syn-D_4 quartz can be calculated using the isotopic fractionation equation for quartz–water of Clayton *et al*. (1972). Considering the formation temperatures of the quartz–scheelite isotope pairs between 208 and 473 °C, the obtained $\delta^{18}O_{water}$ for the aqueous fluid ranges from +9.7 to +12.6‰ (Table 2), which is slightly higher than the $\delta^{18}O_{water}$ value determined from coexisting scheelite and plagioclase during retrograde stage 2. This O isotope composition range indicates more clearly a metamorphic hydrothermal origin of the fluid for the quartz–scheelite assemblage.

Muscovite occurs in D_4-vein haloes (*ca* 275 Ma) and as centrelines in the D_4 veins (*ca* 253 Ma; Poblete *et al*., 2021). The muscovite in the centrelines of veins are paragenetically later than the scheelite, then it is inferred that the muscovite in the vein haloes has also postdated D_4 scheelite. The later timing indicates that the muscovite formation temperatures were lower than that of scheelite. Therefore, the muscovite formation temperatures are inferred to be between 250 and 300 °C. Using the oxygen and hydrogen fractionation equations between muscovite and water (Vennemann & O'Neil, 1996; Zheng, 1993b), the $\delta^{18}O_{water}$ values for the fluid that formed the D_4 muscovite are calculated to range between +8.8 and +11.7‰, and the δD_{water} from −30.1 to −12.3‰. These values are indicative of a metamorphic fluid origin (Figure 12; Taylor, 1974) for the muscovite in the vein haloes and centrelines.

The $\delta^{34}S_{CDT}$ values for retrograde stage 4, D_4-vein sulfides range from −2.5 to +2.8‰ (average of −0.06 ± 1.31‰; Figure 9a). These values are in good agreement with a magmatic source (Ohmoto, 1972) or can also be interpreted to be derived from seawater sulfate. In Figure 13, the right band shows the S isotope compositions of seawater sulfate in geological history, whereas the left band shows the S isotope compositions of sulfides derived from seawater sulfate, also in the geological history. The S isotope composition of Watershed sulfides matches that of the S (in sulfides) derived from Devonian seawater sulfate, the age of the hosting Hodgkinson sedimentary rocks (Adams *et al*., 2013), indicating that the S in the Watershed sulfides could have come from the reduction of Devonian seawater sulfate. As the muscovite O–H isotope compositions are likely metamorphic, it is more likely that the S was derived from seawater sulfate reduction.

Based on evidence obtained from fluid inclusions and stable isotopes, it is proposed that the D_4-vein mineralising system involved mainly metamorphic hydrothermal fluids. The strongest evidence of a metamorphic origin is the $\delta^{18}O$ and $\delta^{18}D$ systematics of vein muscovite, plus the field and mineral textural evidence reported in Poblete *et al*. (2021). Peak metamorphic conditions of upper greenschist to lower amphibolite facies will result in devolatilisation of metasedimentary rocks. The metamorphic hydrothermal model is consistent with the low salinities of the fluids, 0–8 wt% $NaCl_{eq}$. Watershed is not the only metamorphic hydrothermal deposit in the region. There are many orogenic gold deposits in the Hodgkinson Gold Field (Figure 1b) south of Watershed (Peters *et al*., 1990; Vos & Bierlein, 2006) that are metamorphic hydrothermal.

The presence of a magmatic fluid cannot be fully excluded, but stable isotope and fluid inclusion data do not indicate that a magmatic fluid was present. The high geothermal gradient obtained from the *P–T* conditions derived for the trapping of fluids in scheelite and quartz in D_4 veins could be explained by the syn-metamorphism Permian intrusions. The release of heat from these intrusions would increase the geothermal gradient; this does not need the involvement of magmatic water. In the fore-arc environment of a subduction zone, it is not uncommon to have metamorphism and magmatism occurring together [*e.g.,* at Willow Creek, Alaska (Harlan *et al*., 2017), Juneau Gold belt, Alaska (Goldfarb *et al*., 1998; Miller *et al*., 1994), Grass Valley, California (Taylor *et al*., 2015) and Bralorner-Pioneer, British Columbia, Canada (Hart & Goldfarb, 2017)], with the metamorphism caused by the compression from the subduction, and the magmatism also caused by the same subduction, with the magma generation owing to the added water from the serpentinised sea-floor rocks (*e.g.,* Burnham, 1997; Richards & Holm, 2013; Yang *et al*., 2016).

Likewise, the presence of low-salinity meteoric water cannot fully be excluded, but it is unlikely. Typically, meteoric water has a very low salinity, *e.g.*, <1 wt% NaCl. Watershed does have fluid inclusions with <1 wt% $NaCl_{eq}$ salinities that could indicate the presence of meteoric water. However, these fluid inclusions could also represent a metamorphic fluid. Overall, the high pressures and deep formation depths (3.7–6.7 km) of Watershed are not favourable for significant meteoric water or basin brine involvement.

Conclusions

The conclusions of this study are as follows:

1. Using the scheelite–plagioclase isotopic thermometer, the formation temperature of scheelite is 306 ± 56 °C, which is identical to the calculated scheelite–quartz temperature of 307 ± 82 °C, also based on the oxygen isotopes pairs, indicating that scheelite and quartz precipitated synchronously during retrograde stage 2 of D_4 (Table 2). This is consistent with the geological observation of the paragenesis stages.
2. The D_4-vein scheelite formation pressures are calculated to be 1–1.8 kbar, using the H_2O–NaCl FIAs, the above formation temperatures and their calculated isochores. Such pressures give a formational depth between 3.7 and 6.7 km. These variably *P–T* conditions represent the stress variability during D_4 under which the scheelite-rich veins were emplaced. It also shows a variably high geothermal gradient (35–75 °C/km) that may be caused by the heat from the emplacement of Permian magmatic intrusions in the area.
3. D_4-vein scheelite mineralising fluids had low to medium salinities, and both H_2O–NaCl and H_2O–NaCl–CH_4 (X_{CH_4} <0.01) compositions. There is no evidence for fluid–fluid immiscibility. Fluid-inclusion data show evidence of fluid–fluid mixing indicating the presence of a low- (close to 0 wt% $NaCl_{eq}$) and medium-saline fluid (8 wt% $NaCl_{eq}$). There is no evidence indicating which of those two fluids contained CH_4.
4. The presence of sulfide mineral phases, and graphite and CH_4 in some of the fluid inclusions indicates reduced mineralisation conditions.
5. The calculated $\delta^{18}O_{water}$ and δD_{water} of muscovite indicate a metamorphic fluid origin. The calculated $\delta^{18}O_{water}$ of the scheelite–plagioclase pair is inconclusive in determining whether fluids were metamorphic or magmatic; however, the calculated $\delta^{18}O_{water}$ of the scheelite–quartz pair reveals a clear metamorphic hydrothermal origin of the fluid. The S isotopes of the sulfides are consistent with a seawater sulfate source of sulfur. The CH_4 was likely derived from the organic carbon in the carbonaceous slate/slate–siltstone breccia.

Acknowledgements

This study is part of a research project entitled 'Characterising and assessing prospectivity of intrusion-related hydrothermal mineral systems in northeast Queensland' at the Economic Geology Research Centre, James Cook University, in collaboration with the Geological Survey of Queensland, Department of Natural Resources, Mines and Energy, Queensland, under the Future Resources Program. We are grateful to Vital Metals Ltd. for providing the access to the deposit and the logistical support. Robert Skrzeczynsky is thanked for allowing us to use his geological map that forms the base for Figure 2. The authors appreciate very much the valuable discussions with Richard Goldfarb and Vital Metals geologists, and the comments from editor Carl Spandler and two anonymous reviewers that significantly improved this manuscript.

Disclosure statement

No potential conflict of interest was reported by the authors.

Funding

The research reported here was funded by the Geological Survey of Queensland, Department of Natural Resources, Mines and Energy, Queensland, under the Future Resources Program.

ORCID

J. A. Poblete http://orcid.org/0009-0001-3935-2703
J-M. Huizenga http://orcid.org/0000-0003-3254-702X
P. Dirks http://orcid.org/0000-0002-1582-1405

Data availability statement

The data that support the findings of this study are openly available in the supplemental data Table S1 and S2.

References

Adams, C. J., Wormald, R., & Henderson, R. A. (2013). Detrital zircons from the Hodgkinson Formation: Constraints on its maximum depositional age and provenance. In P. A. Jell (Ed.), *Geology of Queensland* (pp. 239–241). Geological Survey of Queensland.

Amos, B. J. (1968). The structure of the Palaeozoic sediments of the Mossman and Cooktown areas, north Queensland. *Journal of the Geological Society of Australia*, *15*(2), 195–208. https://doi.org/10.1080/00167616808728694

Ault, W. V. (1963). Summary of sulfur isotope standards. In M. L. Jensen (Ed.), *Biogeochemistry of sulfur isotopes, National Science Foundation Symposium Proceedings* (pp. 509–567). Yale University.

Bodnar, R. J., Lecumberri-Sanchez, P., Moncada, D., & Steele-MacInnis, M. (2014). Fluid inclusions in hydrothermal ore deposits. In H. D. Holland & K. K. Turekian (Eds.), *Treatise on geochemistry* (2nd ed., Vol. 13, pp. 119–142). https://doi.org/10.1016/B978-0-08-095975-7.01105-0

Bodnar, R. J., & Vityk, M. O. (1994). Interpretation of microthermometric data for H_2O–NaCl fluid inclusions. In B. De Vivo & M. L. Frezzotti (Eds.), *Minerals, methods and applications* (pp. 117–130). Virginia Tech.

Brown, P. E., Bowman, J. R., & Kelly, W. C. (1985). Petrologic and stable isotope constraints on the source and evolution of skarn-forming fluids at Pine Creek, California. *Economic Geology*, *80*(1), 72–95. https://doi.org/10.2113/gsecongeo.80.1.72

Bultitude, R. J., & Champion, D. C. (1992). *Granites of the eastern Hodgkinson Province – Their field and petrographic characteristics.* Queensland Resource Industries Record 1992/6. Geological Survey of Queensland. https://geoscience.data.qld.gov.au/data/report/cr040898

Burnham, C. W. (1997). Magmas and hydrothermal fluids. In H. L. Barnes (Ed.), *Geochemistry of hydrothermal ore deposits* (3rd ed., pp. 63–123). John Wiley and Sons.

Campbell, A. R., & Larson, P. B. (1998). Introduction to stable isotope applications in hydrothermal systems. In J. P. Richards & P. B. Larson (Eds.), *Techniques in hydrothermal ore deposits geology. Reviews in economic geology* (Vol. 10, pp. 173–193). Society of Economic Geologists.

Cattalani, S., & Williams-Jones, A. E. (1991). C–O–H–N fluid evolution at Saint-Robert, Quebec; implications for W–Bi–Ag mineral deposition. *Canadian Mineralogist*, *29*, 435–452.

Champion, D. C., & Bultitude, R. J. (2013). Kennedy Igneous Association. In P. A. Jell (Ed.), *Geology of Queensland* (pp. 473–514). Geological Survey of Queensland, State of Queensland.

Chang, Z., Clarke, G., Cheng, Y., Poblete, J., & Liu, K. (2017). Sn–W–Mo mineralisation in north-east Queensland. In N. Phillips (Ed.), *Australian ore deposits monograph* (Vol. 32, pp. 681–688). Australasian Institute of Mining and Metallurgy.

Chang, Z., Large, R. R., & Maslennikov, V. (2008). Sulfur isotopes in sediment-hosted orogenic gold deposits; evidence for an early timing and a seawater sulfur source. *Geology*, *36*(12), 971–974. https://doi.org/10.1130/G25001A.1

Chang, Z., Shu, Q., & Meinert, L. D. (2019). Skarn deposits of China. In Z. Chang & R. J. Goldfarb (Eds.), *Mineral deposits of China: Society of Economic Geologists Special Publication* (Vol. 22, pp. 189–234). Society of Economic Geologists.

Cheilletz, A. (1984). Caractéristiques géochimiques et thermobarométriques des fluides associés à la scheelite et au quartz des minéralisations de tungstène du Jbel Aouam (Maroc Central). *Bulletin de Minéralogie*, *107*(2), 255–272. https://doi.org/10.3406/bulmi.1984.7757

Clayton, R. N., O'Neil, J. R., & Mayeda, T. K. (1972). Oxygen isotope exchange between quartz and water. *Journal of Geophysical Research*, *77*(17), 3057–3067. https://doi.org/10.1029/JB077i017p03057

Craig, H. (1961). Isotopic variations in meteoric waters. *Science*, *133*(3465), 1702–1703. https://doi.org/10.1126/science.133.3465.1702

Davis, B. K. (1993). Mechanism of emplacement of the Cannibal Creek Granite with special reference to timing and deformation history of the aureole. *Tectonophysics*, *224*(4), 337–362. https://doi.org/10.1016/0040-1951(93)90037-K

Davis, B., Bell, C., Lindsay, M., & Henderson, R. (2002). A single late orogenic Permian episode of gold mineralization in the Hodgkinson province, north Queensland, Australia. *Economic Geology*, *97*(2), 311–323. https://doi.org/10.2113/97.2.311

Davis, B. K., & Henderson, R. A. (1999). Syn-orogenic extensional and contractional deformation related to granite emplacement in the northern Tasman orogenic zone, Australia. *Tectonophysics*, *305*(4), 453–475. https://doi.org/10.1016/S0040-1951(99)00032-3

de Keyser, F., & Lucas, K. G. (1968). *Geology of the Hodgkinson and Laura Basins, North Queensland*. Department of National Development, Bureau of Mineral Resources, Geology and Geophysics.

Donchak, P. J. T., Purdy, D. J., Withnall, I. W., Blake, P. R., & Jell, P. A. (2013). New England Orogen. In P. A. Jell (Ed.), *Geology of Queensland* (pp. 305–472). Geological Survey of Queensland.

Elliott, J. E., Kamilli, R. J., Miller, W. R., & Livo, E. K. (1995). Vein and Greisen Sn and W deposits. In E. A. du Bray (Ed.), *Preliminary compilation of descriptive geoenvironmental mineral deposit models* (pp. 62–69). U. S. Geological Survey Open-File Book 95-831.

Fergusson, C. L., & Henderson, R. A. (2013). Thomson Orogen. In P. A. Jell (Ed.), *Geology of Queensland* (pp. 113–224). Geological Survey of Queensland.

Frezzotti, M. L., Tecce, F., & Casagli, A. (2012). Raman spectroscopy for fluid inclusion analysis. *Journal of Geochemical Exploration*, *112*, 1–20. https://doi.org/10.1016/j.gexplo.2011.09.009

Goldfarb, R. J., Baker, T., Dubé, B., Groves, D. I., Hart, C. J. R., & Gosselin, P. (2005). Distribution character, and genesis of gold deposits in metamorphic terranes. In J. W. Hedenquist, J. F. H. Thompson, R. J. Goldfarb, & J. P. Richards (Eds.), *Economic geology 100th anniversary volume 1905–2005* (pp. 407–450). Society of Economic Geologists.

Goldfarb, R. J., & Groves, D. I. (2015). Orogenic gold; common or evolving fluid and metal sources through time. *Lithos*, *233*, 2–26. https://doi.org/10.1016/j.lithos.2015.07.011

Goldfarb, R. J., Phillips, G. N., Nokleberg, W. J., & Arne, D. C. (1998). Tectonic setting of synorogenic gold deposits of the Pacific Rim. *Ore Geology Reviews*, *13*(1-5), 185–218. https://doi.org/10.1016/S0169-1368(97)00018-8

Goldstein, R. H., & Reynolds, T. J. (1994). *Systematics of fluid inclusions in diagenetic minerals*. SEPM Society for Sedimentary Geology.

Groves, D. I. (1993). The crustal continuum model for late-Archaean lode-gold deposits of the Yilgarn Block, Western Australia. *Mineralium Deposita*, *28*(6), 366–374. https://doi.org/10.1007/BF02431596

Groves, D. I., Goldfarb, R. J., Gebre-Mariam, M., Hagemann, S. G., Robert, F., & Arne, D. C. (1998). Orogenic gold deposits; a proposed classification in the context of their crustal distribution and relationship to other gold deposit types. *Ore Geology Reviews*, *13*(1-5), 7–27. https://doi.org/10.1016/S0169-1368(97)00012-7

Harlan, S. S., Vielreicher, R. M., Mortensen, J. M., Bradley, D. C., Goldfarb, R. J., Snee, L. W., & Till, A. B. (2017). Geology and timing of ore formation in the Willow Creek gold district, Talkeetna Mountains, southern Alaska. *Economic Geology*, *112*(5), 1177–1204. https://doi.org/10.5382/econgeo.2017.4506

Hart, C. J. R., & Goldfarb, R. J. (2017). *Constraints on the metallogeny and geochronology of the Bridge River Gold District and Associated Intrusions, southwestern British Columbia (NTS 092J/15)* (Geoscience British Columbia Report 2017-08).

Henderson, R. A., Donchak, P. J. T., & Withnall, I. W. (2013). Mossman Orogen. In P. A. Jell (Ed.), *Geology of Queensland* (pp. 225–304). Geological Survey of Queensland.

Henley, R. W., Norris, R. J., & Paterson, C. J. (1976). Multistage ore genesis in the New Zealand geosyncline; a history of post-metamorphic lode emplacement. *Mineralium Deposita*, *11*(2), 180–196. https://doi.org/10.1007/BF00204480

Hurai, V. (2010). Fluid inclusion geobarometry: Pressure corrections for immiscible H_2O–CH_4 and H_2O–CO_2 fluids. *Chemical Geology*, *278*(3-4), 201–211. https://doi.org/10.1016/j.chemgeo.2010.09.014

Kositcin, N., Purdy, D. J., Brown, D. D., Bultitude, R. J., & Carr, P. A. (2015). *Summary of results Joint GSQ–GA geochronology project: Thomson Orogen and Hodgkinson Province, 2012–2013* (Geological Survey of Queensland Record 2015/02).

Kwak, T. A. P. (1986). Fluid inclusions in skarns (carbonate replacement deposits). *Journal of Metamorphic Geology*, *4*(4), 363–384. https://doi.org/10.1111/j.1525-1314.1986.tb00358.x

Kwak, T. A. P. (1987). *W–Sn skarn deposits and related metamorphic skarns and granitoids*. Elsevier, Developments in Economic Geology (Vol. 24).

Mackenzie, D. E., & Wellman, P. (1997). Kennedy Province. In J. H. C. Bain & J. J. Draper (Eds.), *North Queensland geology. AGSO Bulletin 240/ Queensland Geology 9* (pp. 488–500). Australian Geological Survey Organisation, Canberra & Queensland Department of Mines and Energy.

Meinert, L. D., Dipple, G. M., & Nicolescu, S. (2005). World Skarn deposits. In J. W. Hedenquist, J. F. H. Thompson, R. J. Goldfarb, & J. P. Richards (Eds.), *Economic geology 100th anniversary volume 1905–2005* (pp. 229–336). Society of Economic Geologists.

Miller, L. D., Goldfarb, R. J., Gehrels, G. E., & Snee, L. W. (1994). Genetic links among fluid cycling, vein formation, regional deformation, and plutonism in the Juneau gold belt, southeastern Alaska. *Geology*, *22*(3), 203–206. https://doi.org/10.1130/0091-7613(1994)0222.3.CO;2

Newberry, R. J. (1998). W- and Sn-skarn deposits: A 1998 status report. In D. R. Lentz (Ed.), *Mineralized intrusion-related systems* (Vol. 26, pp. 289–335). Mineralogical Association of Canada Short Course.

Newberry, R. J., & Swanson, S. E. (1986). Scheelite skarn granitoids; an evaluation of the roles of magmatic source and process. *Ore Geology Reviews*, *1*(1), 57–81. https://doi.org/10.1016/0169-1368(86)90005-3

Ohmoto, H. (1972). Systematics of sulfur and carbon isotopes in hydrothermal ore deposits. *Economic Geology*, *67*(5), 551–578. https://doi.org/10.2113/gsecongeo.67.5.551

Peters, S. G., Golding, S. D., & Dowling, K. (1990). Melange- and sediment-hosted gold-bearing quartz veins, Hodgkinson gold field, Queensland, Australia. *Economic Geology*, *85*(2), 312–327. https://doi.org/10.2113/gsecongeo.85.2.312

Poblete, J. A., Dirks, P. H. G. M., Chang, Z., Huizenga, J. M., Griessmann, M., & Hall, C. (2021). The Watershed tungsten deposit, northeast Queensland, Australia; Permian metamorphic tungsten mineralization overprinting Carboniferous magmatic tungsten. *Economic Geology*, *116*(2), 427–451. https://doi.org/10.5382/econgeo.4791

Ramboz, C., Pichavant, M., & Weisbrod, A. (1982). Fluid immiscibility in natural processes; use and misuse of fluid inclusion data: II. Interpretation of fluid inclusion data in terms of immiscibility. *Chemical Geology*, *37*(1-2), 29–48. https://doi.org/10.1016/0009-2541(82)90065-1

Ramboz, C., Schnapper, D., & Dubessy, J. (1985). The *P–V–T–X–fO2* evolution of H_2O–CO_2–CH_4-bearing fluid in a wolframite vein: Reconstruction from fluid inclusion studies. *Geochimica et Cosmochimica Acta*, *49*(1), 205–219. https://doi.org/10.1016/0016-7037(85)90205-4

Richards, S. W., & Holm, R. J. (2013). Tectonic preconditioning and the formation of giant porphyry deposits. In M. Colpron, T. Bissig, B. G. Rusk, & J. F. H. Thompson (Eds.), *Tectonics, metallogeny, and discovery: The North American Cordillera and similar accretionary settings* (pp. 265–275). Society of Economic Geologists Special Publication 17.

Roedder, E., & Bodnar, R. J. (1980). Geologic pressure determinations from fluid inclusion studies. *Annual Review of Earth and Planetary Sciences*, *8*(1), 263–301. https://doi.org/10.1146/annurev.ea.08.050180.001403

Schenk, P., & Höll, R. (1991). Evolution of fluids and metamorphic ore remobilization in the Felbertal scheelite deposit, Eastern Alps. *Ore Geology Reviews*, *6*(5), 425–434. https://doi.org/10.1016/0169-1368(91)90039-A

Setzmann, U., & Wagner, W. (1991). A new equation of state and tables of thermodynamic properties for methane covering the range from the melting line to 625 K at pressures up to 1000 MPa. *Journal of Physical and Chemical Reference Data*, *20*(6), 1061–1155. https://doi.org/10.1063/1.555898

Shanks, W. C. P. (2014). Stable isotope geochemistry of mineral deposits. In H. D. Holland & K. K. Turekian (Eds.), *Treatise on geochemistry* (2nd ed., Vol. 13, pp. 59–85). Elsevier. https://doi.org/10.1016/B978-0-08-095975-7.01103-7

Sharp, Z. D. (1990). A laser-based microanalytical method for the *in situ* determination of oxygen isotope ratios of silicates and oxides. *Geochimica et Cosmochimica Acta*, *54*(5), 1353–1357. https://doi.org/10.1016/0016-7037(90)90160-M

Shimazaki, H. (1980). Characteristics of skarn deposits and related acid magmatism in Japan. *Economic Geology*, *75*(2), 173–183. https://doi.org/10.2113/gsecongeo.75.2.173

Skrzeczynski, R. H., & Wood, A. M. (1984). *Annual report for 1983 on authority to prospect 3227M Maitland Dows Area North Queensland Report No. 391 Volume 1*. Geological Survey of Queensland. https://geoscience.data.qld.gov.au/data/report/cr013146

So, C-S., & Shelton, K. L. (1983). A sulfur isotopic and fluid inclusion study of the Cu–W-bearing tourmaline breccia pipe, Ilkwang Mine, Republic of Korea. *Economic Geology*, *78*(2), 326–332. https://doi.org/10.2113/gsecongeo.78.2.326

Steele-MacInnis, M., Lecumberri-Sanchez, P., & Bodnar, R. J. (2012). HokieFlincs_H_2O–NaCl: A Microsoft Excel spreadsheet for interpreting microthermometric data from fluid inclusions based on the PVTX properties of H_2O–NaCl. *Computers & Geosciences*, *49*, 334–337. https://doi.org/10.1016/j.cageo.2012.01.022

Taylor, H. P. (1974). The application of oxygen and hydrogen isotope studies to problems of hydrothermal alteration and ore deposition. *Economic Geology*, *69*(6), 843–883. https://doi.org/10.2113/gsecongeo.69.6.843

Taylor, R. D., Goldfarb, R. J., Monecke, T., Fletcher, I. R., Cosca, M. A., & Kelly, N. M. (2015). Application of U–Th–Pb phosphate geochronology to young orogenic gold deposits: New age constraints on the formation of the Grass Valley Gold District, Sierra Nevada Foothills Province, California. *Economic Geology*, *110*(5), 1313–1337. https://doi.org/10.2113/econgeo.110.5.1313

Vennemann, T. W., & O'Neil, J. R. (1996). Hydrogen isotope exchange reactions between hydrous minerals and molecular hydrogen: I. A new approach for the determination of hydrogen isotope fractionation at moderate temperatures. *Geochimica et Cosmochimica Acta*, *60*(13), 2437–2451. https://doi.org/10.1016/0016-7037(96)00103-2

Vos, I. M. A., & Bierlein, F. P. (2006). Characteristics of orogenic-gold deposits in the Northcote District, Hodgkinson Province, north Queensland: Implications for tectonic evolution. *Australian Journal of Earth Sciences*, *53*(3), 469–484. https://doi.org/10.1080/08120090600632474

Wesolowski, D., & Ohmoto, H. (1986). Calculated oxygen isotope fractionation factors between water and the minerals scheelite and powellite. *Economic Geology*, *81*(2), 471–477. https://doi.org/10.2113/gsecongeo.81.2.471

Whitney, D. L., & Evans, B. W. (2010). Abbreviations for names of rock-forming minerals. *American Mineralogist*, *95*(1), 185–187. https://doi.org/10.2138/am.2010.3371

Wilkinson, J. J. (2001). Fluid inclusions in hydrothermal ore deposits. *Lithos*, *55*(1-4), 229–272. https://doi.org/10.1016/S0024-4937(00)00047-5

Wilkinson, J. J. (2017). Metastable freezing; a new method for the estimation of salinity in aqueous fluid inclusions. *Economic Geology*, *112*(1), 185–193. https://doi.org/10.2113/econgeo.112.1.185

Withnall, I. W., & Hutton, L. J. (2013). North Australian Craton. In P. A. Jell (Ed.), *Geology of Queensland* (pp. 23–112). Geological Survey of Queensland, State of Queensland.

Wood, S. A., & Samson, I. M. (2000). The hydrothermal geochemistry of tungsten in granitoid environments; I, Relative solubilities of ferberite and scheelite as a function of T, P, pH, and mNaCl. *Economic Geology*, *95*(1), 143–182. https://doi.org/10.2113/gsecongeo.95.1.143

Yang, Z., Goldfarb, R., & Chang, Z. (2016). Generation of post-collisional porphyry Cu deposits in southern Tibet triggered by subduction of Indian continental plate. In J. P. Richards (Ed.), *Special publication number 19 Tectonics and metallogeny of the Tethyan orogenic belt* (pp. 279–300). Society of Economic Geologists.

Zheng, Y-F. (1993a). Calculation of oxygen isotope fractionation in anhydrous silicate minerals. *Geochimica et Cosmochimica Acta*, *57*(5), 1079–1091. https://doi.org/10.1016/0016-7037(93)90042-U

Zheng, Y-F. (1993b). Calculation of oxygen isotope fractionation in hydroxyl-bearing silicates. *Earth and Planetary Science Letters*, *120*(3-4), 247–263. https://doi.org/10.1016/0012-821X(93)90243-3